Energy Conversion and Management 291 (2023) 116985

Contents lists available at ScienceDirect

Energy Conversion and Management

journal homepage: www.elsevier.com/locate/enconman

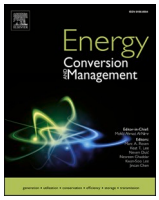

Integration of a novel Chemical Looping Combustion reactor into a thermochemical energy storage system

M. Astolfi [a,*], M.E. Diego [b], M. Romano [a], J.C. Abanades [b]

[a] Politecnico di Milano, Department of Energy, via Lambruschini 4, 20156 Milan, Italy
[b] Instituto de Ciencia y Tecnología del Carbono (INCAR), CSIC, Francisco Pintado Fe 26, 33011 Oviedo, Spain

ARTICLE INFO

Keywords:
Energy storage
Decarbonized electricity
Chemical looping
CO_2 capture
System integration
Back-up power

ABSTRACT

This study analyses the performance of a back-up power process that uses a novel chemical looping packed bed air reactor to oxidize a batch of reduced solids while heating high pressure flowing air. In this arrangement, the solids are slowly oxidized by a diffusionally-controlled flow of oxygen perpendicular to the main air flow, thus imposing very long oxidation times for all reacting particles. A decay in the thermal power output of the reactor can be expected with time due to the increasing resistance to O_2 diffusion towards the unreacted oxygen carrier particles as the reaction progresses. In this work, integration of the dynamic system formed by the reactor and the power plant used to produce power from the exploitation of the variable thermal output of the reactor is investigated. Different case studies are assessed for decarbonization of energy production and storage of renewable energy. The reactor is rated at a maximum 50 MW_{th} power output in all cases, employing iron- or nickel-based particles as oxygen carrier. A simplified model for mass and heat transfer in the proximity of the wall orifices allows the definition of operating windows and reactor dimensions. In the chosen case examples, each single reactor operates in discharge mode for around 4–5 h (depending on plant configuration) as a back-up power generator, heating up a compressed air stream up to ~ 1000 °C and achieving an energy density between 816 and 2214 kWh_{th}/m^3. Gas turbines in recuperative, steam injected and combined cycle power plant architectures integrated in the novel chemical looping combustion (CLC) reactor are investigated. Cycle efficiencies up to 49% are calculated for systems that make use of a single reactor configuration and exploit the residual heat for power production through a organic Rankine cycle (ORC) bottomed system. A more flexible multi-reactor configuration is also investigated to address the unavoidable decay in power output during discharge and provide power output controllability. The levelized cost of electricity (LCOE) is estimated be comparable to system elements from the literature when H_2 is used as reducing gas. The use of biogas to reduce the solids during the energy charge stage is found to be particularly advantageous, leading to LCOE values between ~ 120 and 175 €/MWh for the reference reactor system using iron-based solids. This also allows achieving negative CO_2 emissions if the captured CO_2 generated during the reduction stage is stored.

1. Introduction

Future electricity systems will require back-up power and energy storage solutions capable of dispatching carbon-free electricity to compensate for intermittency of variable renewable sources and ensure demand is met at all times [1–3]. Commercial scale energy storage systems are nowadays mainly based on electrochemical batteries, that suffer from performance decay over time and limited lifetime or pump hydro and compressed air energy storage (CAES) systems that are only viable at certain geographical locations [4,5]. Moreover, several other energy storage technologies are under development as liquid air energy storage (LAES) [6], CO_2-batteries [7], and pumped thermal energy storage (PTES) based on Brayton cycles [8], CO_2 trans-critical systems [9] and organic Rankine cycles (ORC) [10] which can have a wide range of power and energy ratings [11–13]. Additionally, large efforts are being devoted towards the development of *Power-to-Gas* and *Power-to-Liquid* systems, where H_2 or other synthetic fuels are produced during times of excess renewable energy generation to be stored and used afterwards during peak demand periods [2,11,14]. These are seen as interesting options for sector coupling, although their mitigation potential is limited if fossil CO_2 is employed as precursor for C-based synthetic fuels [15,16]. Amongst these alternatives, this study analyses the performance of a thermochemical back-up power process based on

* Corresponding author.
E-mail address: marco.astolfi@polimi.it (M. Astolfi).

https://doi.org/10.1016/j.enconman.2023.116985
Received 8 February 2023; Received in revised form 27 March 2023; Accepted 29 March 2023
Available online 11 July 2023

Nomenclature

A_c	Cross sectional wall area associated to an orifice within a control volume of the reactor, m^2
A_{HRSG}	Heat transfer area of the heat recovery steam generator, m^2
A_{REC}	Heat transfer area of the recuperator, m^2
BOP	Balance of plant, M€
CAES	Compressed air energy storage
CAPEX	Capital expenditure, M€
CC	Combined cycle
CCF	Carrying Charge Factor
c_{ES}	Specific fuel charging cost, €/MWh_{th}
c_f	Cost of fuel, €/kg
CCHP	combined cooling heating and power
$C_{O2\ bulk,i}$	Local oxygen concentration in the bulk gas flow, mol/m^3
$C_{O2\ r,i}$	Local oxygen concentration at the reaction front, mol/m^3
$C_{O2\ w,i}$	Local oxygen concentration at the inner side of the wall in contact with the solids, mol/m^3
$C_{p\ gas,i}$	Local specific heat capacity of the gas, J/kg·K
CS	Constant Speed
CT	Carbon tax, €/ton $_{CO2}$
$D_{O2,i}$	Local diffusivity of oxygen in air, m^2/s
e	Stoichiometric oxygen needed to oxidize the reduced solids, mol O_2/kg
E_{el}	Net electric energy output, MWh_{el}
$E_{elD,y}$	Electrical energy produced in the discharging process at year *y,* MWh_{el}
$E_{thC,y}$	Energy stored in the reactor during the charging process at year *y,* MWh_{th}
$E_{thD,y}$	Thermal energy released in the discharging process at year *y,* MWh_{th}
$E_{el,ORC}$	Electric energy output of the ORC cycle, MW_{el}
$E_{el,pump}$	Electrical water pump energy consumption in the STIG configuration, MW_{el}
$E_{el,TG}$	Electric energy output of the gas turbine cycle, MW_{el}
h_i	Local heat transfer coefficient, W/m^2·K
LAES	Liquid Air Energy Storage
LCOE	Levelised cost of produced energy, €/MWh_{el}
$LCOE_{system}$	Levelised cost of produced energy related to the power block and reactor, €/MWh_{el}
LHV	Fuel lower heating value, MWh_{th}/kg
$L_{r,i}$	Local position of the reactor front, m
L_w	Thickness of the porous wall of the gas conduits, m
N	Plant lifetime, years
$N_{O2,i}$	Moles of O_2, mol
m_{air}	Air mass flow rate at compressor inlet, kg/s
m_i	Local mass flow of gases, kg/s
$m_{C,n}$	Nominal compressor intake air mass flow rate, kg/s
$m_{T,n}$	Nominal mass flow rate at turbine inlet, kg/s
m_{offD}	Fluid mass flow rate in off-design conditions, kg/s
m_{onD}	Fluid mass flow rate in nominal conditions, kg/s
$m_{gas,in}$	Gas mass flow rate at reactor inlet, kg/s
$m_{r,T}$	Reduced mass flow rate at turbine inlet, kg/s
m_{vap}	Steam mass flow rate in the STIG case, kg/s
NR	Number of active reactors in a multireactor configuration
OPEX	Operational expenditure, M€
$OPEX_{fix}$	Fixed operational expenditure, M€
$OPEX_{var}$	Variable operational expenditure, €/MWh_e
ORC	Organic Rankine Cycle
$p_{in,T}$	Turbine inlet pressure, bar
Q_{gas}	Power used to heat up the gases leaving the reactor, W
Q_{low}	Lower bound of multireactor discharge operation window, W
Q_{max}	Maximum thermal power that could be supplied by the multireactor system at any time by modifying the configuration of active/inactive reactors available at any moment, W
Q_{min}	Minimum thermal power that could be supplied by the multireactor system at any time by modifying the configuration of active/inactive reactors available at any moment, W
$Q_{ox,i}$	Local power generated during oxidation, W
$Q_{O2,preheat}$	Power used to preheat the diffusion oxygen passing through the wall, W
$Q_{reaction}$	Total oxidation power, W
Q_t	Thermal power released at time *t* during discharge when using a multireactor configuration, W
Q_{thres}	Minimum total thermal power that the multireactor configuration shall provide after a configuration switch during discharge, W
Q_{up}	Upper bound of multireactor discharge operation window, W
PTES	Pumped Thermal Energy Storage
r	Discount rate, %
REC	Recuperative
SOC	State of charge
$SOC_{i,t}$	State of charge of reactor *i* at time *t* in a multireactor configuration
$\bar{SOC}_t$	Average state of charge of the reactors in a multireactor configuration at time *t*
STIG	Steam Injected Gas turbine
t	Time, s
TASC	Total as spent cost, M€
TGA	ThermoGravimetric Analysis
$T_{gas,i}$	Local gas temperature, °C
$T_{gas,in}$	Temperature at reactor inlet, °C
$T_{gas,in,\ min}$	Minimum temperature at reactor inlet, °C
$T_{in,T}$	Turbine inlet temperature, °C
$T_{w,i}$	Local wall temperature, °C
VIGV	Variable Inlet Guide Vanes
VS	Variable Speed
$W_{el,ORC}$	Electrical power produced by the ORC, W
$W_{el,pump}$	Electrical power consumption of the water pump in the STIG configuration, W
$W_{el,TG}$	Electrical power produced by the gas turbine cycle, W
$x_{O2,in}$	Oxygen molar fraction at reactor inlet

Greek symbols

β_C	Actual compressor pressure ratio
$\beta_{C,n}$	Nominal compressor pressure ratio
β_T	Turbine pressure ratio
$\beta_{T,n}$	Nominal turbine pressure ratio
Δh_{ratio}	Ratio between the LHV of the fuel and the heat of the oxidation reaction
ΔH_{ox}	Oxidation enthalpy, kJ/mol
ΔSOC	Maximum difference in the state of charge of any reactor with respect to the average reactors state of charge in a multireactor configuration
ΔT_{min}	Minimum temperature difference, °C
ε_s	Bed porosity
ε_w	Orifice fraction in the gas conduit walls
η_r	Reactor charging efficiency
$\bar{\eta}_{pb,y}$	Average power block conversion efficiency
$\rho_{OC,red}$	Density of the reduced oxygen carrier, kg/m^3
$\upsilon_{OC,red}$	Volume fraction of active oxygen carrier in the bed

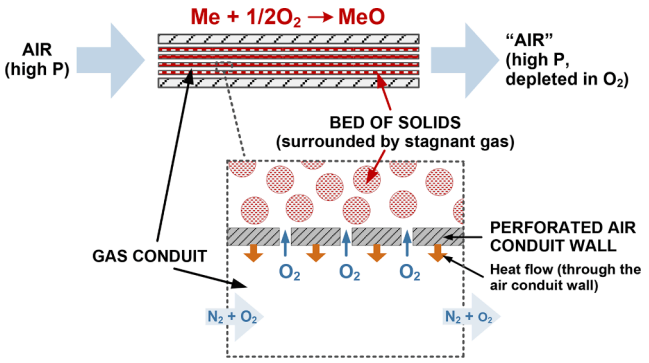

Fig. 1. Representation of the proposed air CLC reactor integrated and detail on the main oxygen and thermal fluxes around the orifices of the perforated conduit walls during discharge (oxidation) periods adapted from [35].

chemical looping combustion (CLC) principles.

CLC processes make use of an oxygen carrier material (typically metallic, e.g. Fe-, Ni-, Cu-, Mn-based, etc.) that is used to transfer oxygen from combustion air to a fuel, without direct contact between them. Thereby, the reduced oxygen carrier is first oxidized to *MeO* using air in discharging phase, to be then reduced back to *Me* during fuel combustion in charging phase. Development of the CLC technology has been mainly focused on CO_2 capture applications [17,18] possibly with hydrogen production [19] and integration with CCHP (combined cooling heating and power) systems [20]. Moreover, the use of CLC for thermochemical energy storage purposes as been already described in detail by some literature review papers [21–23], and addressed from both numerical and experimental point of view. Relevant experimental activities has been carried out on the characterization in TGA apparatus of Manganese-Titanium mixed oxides with mass fractions of Titanium from 0 to 50% [24], cycling stability of Manganese-Silicon oxide having silica content between 2% and 10% [25], cycling stability for CuO/Cu_2O [26] and characterization of the potential of Fe_3O_4-CaO [27] and F_2O_3 [28,29]. In addition, numerical studies have been presented on several oxygen carries (i.e. Fe_3O_4-CaO [30] or Aluminum and Sodium [31]) also coupled with concentrating solar power [32,33] and integrated with hydrogen production [34].

Most of these studies are focused on the oxygen carrier performance when cycling between reducing and oxidizing conditions during energy storage and supply periods, respectively. Nevertheless, further investigations into new process and reactor schemes are necessary to progress on the development and future deployment of the chemical looping energy storage concept at large scale.

A new chemical looping packed bed reactor concept is at the core of the thermochemical back-up power system investigated in this work, where a batch of reduced *Me* solids is oxidized while heating high pressure flowing air [35,36], as shown in Fig. 1. By using a packed bed reactor configuration [37], operational issues related to the use of pressurized interconnected CLC fluidized bed reactors (i.e. difficulties in maintaining a stable circulation of solids between reactors and the possibility of particles being entrained with the exiting gas, hence damaging the downstream gas turbine [18,38]) are avoided. In this system, the reactor is designed to allow a very large bypass of unconverted oxygen by avoiding the direct contact of air with the solids. As seen in Fig. 1, air flows through longitudinal gas conduits that are empty of solids, but their walls have orifices/pores making them permeable but non-selective to gases. *Me* solids are slowly oxidized by a diffusionally-controlled flow of oxygen perpendicular to the main air flow, which is driven by the oxygen concentration gradient between the O_2-rich gas flowing through the conduits and the O_2-depleted stagnant gas surrounding the reduced particles as given by Fick's law of diffusion. This arrangement imposes very long oxidation times for all reacting particles [39]. As a result, appearance of hot spots and sharp temperature profiles in the bed, that typically occur in chemical looping packed bed reactor configurations, is avoided without the need for dedicated heat management strategies [40,41]. Discharge periods are followed by charge stages where the oxidized *MeO* solids are reduced back to *Me*. Reduction may also proceed as a diffusionally-controlled process inside the reactor, employing either fossil or renewable fuel gases. Depending on the reducing gas choice, two potential applications are distinguished for this technology and investigated in this work:

- **Case A: decarbonization of energy production.** In this case, fossil (natural gas) or carbon-containing renewable gases (biogas, landfill gas, other opportunity gas) are used during charging stages to reduce *MeO* solids back to *Me*. As depicted in Fig. 2, reduction product gases are mainly H_2O_v and/or CO_2, leading to a high purity CO_2 stream ready for storage or use after water condensation and purification in a CPU. Furthermore, negative CO_2 emissions can be achieved by permanently storing the CO_2 produced when a carbon-based renewable reducing gas is employed during charging stages.
- **Case B: storage of renewable energies**. The CLC system of Fig. 1 is proposed as an alternative solution to green hydrogen storage in large pressurized vessels (see Fig. 2). In this case, hydrogen is stored in the form of a reduced *Me* oxygen carrier, with H_2O_v being the only gas produced during reduction. Steam, after condensation can be used again for the electrolyzer leading to a zero water consumption system representing an additional value in charging periods (summer) or geographical locations characterized by water scarcity.

The design of the reactor of Fig. 1 is largely dependent on the discharge (oxidation) stage requirements, such as the targeted power output and discharge times, as well as on the oxygen carrier choice, which affects the maximum gas temperature at reactor outlet and the energy density of the device. In principle, any oxygen carrier (OC) material can be used in this reactor type, although inexpensive solids with large volumetric oxygen carrier capacity are favored from technoeconomic perspective. Oxidation of the *Me* solids in the reactor

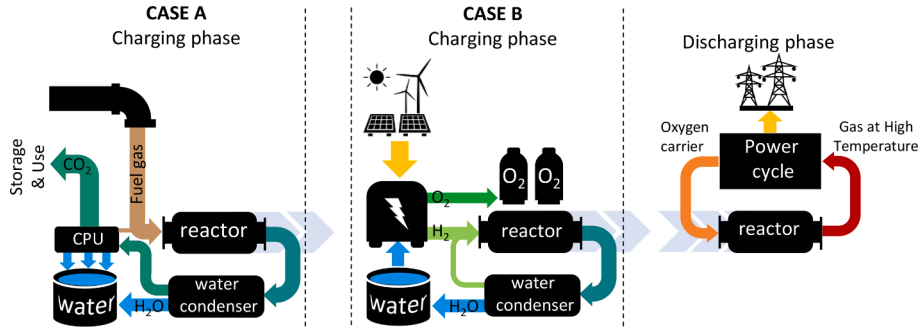

Fig. 2. Cases investigated in the present work. Case A: decarbonization of fossil fuels or negative emissions from biogas. Case B: alternative storage solution for green hydrogen. (For interpretation of the references to colour in this figure legend, the reader is referred to the web version of this article.)

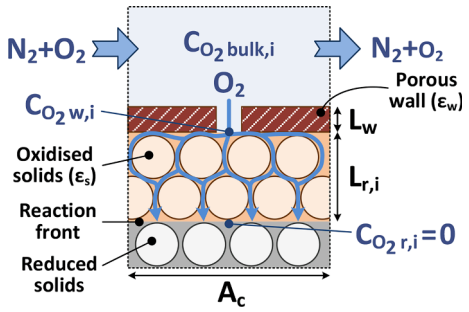

Fig. 3. Schematics of a control volume of the reactor containing the gas and solids associated to an orifice/pore of the conduit wall.

progresses in reaction fronts nearly parallel to the walls of the perforated gas conduits. This causes a decay in the thermal power output of the reactor with time [36] due to the additional resistance imposed by the layer of oxidized solids, which hinders O_2 diffusion towards the unreacted oxygen carrier particles. As the discharge stage progresses, this can be easily compensated for by burning increasing amounts of gaseous fuels at the inlet or outlet of the reactor. However, this strategy comes at the expense of emitting CO_2 to the atmosphere and thus, alternative are the preferred choice when a CO_2-free operation is pursued.

This work presents a comprehensive analysis of the integration of the novel reactor design, using iron- and nickel-based solids as oxygen carrier material, with three different power plants configurations based on gas turbines modified architectures. The overall system has never been presented in this integrated version, nor optimized in detail, nor studied in off design conditions over a whole discharging cycle. Results obtained in this work thus provide new quantification of the technology potential from both thermodynamic and techno economic perspective leading to a fair comparison against other storage technologies. As additional innovation step this work addresses the importance of using multireactor systems to solve the flexibility bottlenecks related to the use of single reactor systems with the definition of some easy to implement management strategies. Finally, the results have been extended to different case studies investigating both the use of biogas, natural gas and green hydrogen.

2. Reactor modeling, design and power decay curve definition

2.1. Reactor mathematical model

A simplified reactor model has been developed to describe the mass and heat transfer phenomena occurring during oxidation of the oxygen carrier, using similar assumptions as in Diego and Abanades [39]. The model uses Fick's law to account for oxygen diffusion through the porous walls of the gas conduits. Furthermore, the oxidation reaction is assumed to progress without any intrinsic kinetic limitation and thus, the small oxygen diffusion flow arriving at the reduced solids reacts instantaneously. As a result, the oxygen concentration in the vicinity of the reacting particles, which are highly reactive towards oxygen, is taken to be zero (see $C_{O2,r} = 0$ in Fig. 3). A mass balance performed to a control volume of the reactor enclosing the gas and solids associated to one orifice/pore of the gas conduit walls (as represented in Fig. 3) allows quantifying the local flow of oxygen diffusing through the wall and reacting with the solids at any time as reported in equation (1):

$$-\frac{dN_{O_{2,i}}}{dt} = D_{O_{2,i}} A_c \varepsilon_w \frac{C_{O_2 bulk,i} - C_{O_2 w,i}}{L_w} = D_{O_{2,i}} A_c \varepsilon_s \frac{C_{O_2 w,i}}{L_{r,i}} \quad (1)$$

where $D_{O2,i}$ is the local diffusivity of oxygen in air, A_c is the cross sectional wall area associated to an orifice, ε_w is the fraction of orifices in the wall, ε_s is the porosity of the bed of reacted particles, L_w is the thickness of the porous wall, $L_{r,i}$ is the position of the reaction front in the reactor control volume i, and $C_{O2\ bulk,\ i}$ and $C_{O2\ w,\ i}$ are the local oxygen concentrations in the bulk gas flow and at the inner side of the wall in contact with the solids, respectively.

Equation (1) can be rearranged in equation (2) to calculate the apparent oxidation reaction rate as a function of the two resistances in series resulting from diffusion through the porous wall and through the bed of reacted solids:

$$-\frac{dN_{O_{2,i}}}{dt} = \frac{D_{O_{2,i}} A_c C_{O_2 bulk,i}}{\frac{L_w}{\varepsilon_w} + \frac{L_{r,i}}{\varepsilon_s}} \quad (2)$$

Moreover, the molar oxygen consumption rate can be also calculated as reported in equation (3):

$$-\frac{dN_{O_{2,i}}}{dt} = A_c \rho_{OC,red} \upsilon_{OC,red} e \frac{dL_{r,i}}{dt} \quad (3)$$

For the sake of simplicity, no swelling or shrinkage of the solids bed is assumed during oxidation in equation (3), where $\rho_{OC,red}$ is the density of the reduced oxygen carrier, $\upsilon_{OC,red}$ is the volume fraction of active oxygen carrier in the bed and e represents the stoichiometric oxygen needed in moles per unit of mass of reduced solids.

Combining equations (2) and (3), it is possible to obtain an expression, reported in equation (4), to calculate the position of the oxidation reaction front at any time as:

$$L_{r,i} = \sqrt{\left(\frac{\varepsilon_s L_w}{\varepsilon_w}\right)^2 + \frac{2 D_{O_{2,i}} \varepsilon_s C_{O_2\ bulk,i}}{\rho_{OC,red} \upsilon_{OC,red} e} t} - \frac{\varepsilon_s L_w}{\varepsilon_w} \quad (4)$$

Similarly, the gas temperature profile in the reactor can be calculated by performing an energy balance. For the sake of simplicity, any dynamic changes in temperature to achieve pseudo-steady states are not considered at this stage since the energy involved is only a small fraction of the oxidation heat released by the solids. Moreover, no radial temperature profiles are assumed in the shallow bed of solids located between gas conduits. Therefore, assuming an adiabatic reactor where the oxidation heat flows from the oxidizing solids perpendicularly through the wall and is entirely used to heat up the flowing air, the evolution of the local gas and wall temperatures, $T_{gas,i}$ and $T_{w,i}$ respectively, can be obtained as a function of the local power generated during oxidation, $Q_{ox,i}$ as reported in equation (5):

$$Q_{ox,i} = -\Delta H_{ox} \frac{dN_{O_{2,i}}}{dt} = m_i C_{pgas,i} dT_{gas,i} = h_i A_c (1 - \varepsilon_w) dT_{w,i} \quad (5)$$

where ΔH_{ox} is the enthalpy of the oxidation reaction, m_i is the mass flow of gases at that point of reactor length, $C_{p\ gas,i}$ is the local specific heat capacity of the gas and h_i represents the local heat transfer coefficient, which can be calculated from the Nusselt number using the Dittus and Boelter correlation.

In this work, the reactor model is solved by dividing the reactor into a series of small reactor elements in the axial direction (each of 0.1 m length), where all the gas and solids variables are assumed to be constant. In this approach, the output variables from a reactor element are employed as inputs to solve the mass and energy balances of the next section.

2.2. Case studies and reactor design

Two main case studies are investigated in this work, involving both decarbonization of energy production when using fossil fuel (natural gas) or renewable reducing gas containing methane (case A) and storage of renewable H_2 chemical energy (case B). For each case, a reactor is designed using the model described above together with the boundary conditions reported in Table 1, which are chosen to ensure the same power decay curve is followed during discharge in all cases (see section 2.3) so that the same power plant design can be used.

A key aspect for reactor design is the oxygen carrier (OC) selection. A promising option is the use of iron-based oxygen carrier materials due to

Table 1
Reference boundary conditions used for the reactor designs and calculated design parameters. (*) Average properties of the iron species after reduction (mixture of 0.01/0.80/0.19 (molar fraction) of Fe_3O_4/FeO/Fe [35]).

CASE	A.1	A.2	B
General assumptions			
Inlet gas temperature, $T_{gas,in}$, °C		550	
Inlet gas velocity, m/s		25	
Inlet gas pressure, atm		5	
Inlet oxygen molar fraction, $x_{O2,in}$		0.21	
Volume fraction of active oxygen carrier		0.3	
Bed porosity, ε_s		0.4	
Thickness of the porous wall, L_w, m		0.001	
Gas conduit height, m		0.016	
Maximum power output, MW_{th}		50	
Maximum discharge time at reference conditions, h		4	
Case-specific assumptions			
Oxygen carrier	Fe/FeO/Fe_3O_4/Fe_2O_3	Ni/NiO	Fe/Fe_2O_3
Oxidation enthalpy, ΔH_{ox}, kJ/mol O_2	547.0*	470.0	553.7
Density of the reduced oxygen carrier, kg/m^3	5962*	8900	7874
Oxygen carrying capacity (kg/kg)	0.136*	0.21	0.30
Orifice fraction in the gas conduit walls, ε_w	0.032	0.052	0.060
Reactor length, m	29	21	15
Calculated reactor design parameters			
Energy storage capacity, MWh_{th}	125	125	125
Number of gas conduits	51	58	60
Cross section, m^2	5.3	4.1	3.8
Inlet mass flow rate, $m_{gas,in}$, kg/s	100	100	100
Energy density, kWh_{th}/m^3	816	1474	2214
Thickness of the solids beds in between gas conduits, m	0.028	0.017	0.015
Maximum discharge temperature, °C	1001	1008	1004

their high oxygen transport capacity (up to 0.3 g O_2/g if the Fe/Fe_2O_3 system is considered), low cost and stability at temperatures over 1000 °C. Due to thermodynamic limitations, full CH_4 or H_2 conversion during charging stages can only be achieved when Fe_2O_3 is reduced back to Fe_3O_4, whereas unconverted gas leaves the system if solids are further reduced to FeO and Fe [42]. In case of fuel gas (Case A.1), only partial reduction of the Fe_2O_3 solids is assumed to occur during charging stages to prevent from unconverted fuel leaving the reactor, i.e. reduction is assumed to be carried out until the last mole of Fe_2O_3 disappears from the bed and then, it is stopped. By doing so, full gas conversion is ensured, since reduction of Fe_2O_3 to Fe_3O_4, FeO and Fe is expected to proceed in sequential reaction fronts in the reactor (see discussion elsewhere [35]). This solution allows obtaining a stream at the outlet of the reactor that can be easily enriched in CO_2 simply by water condensation, thus avoiding the use of more costly purification systems to separate and recirculate unconverted fuel gas. However, this comes at the expense of a reduction in the energy density of the reactor, since a mixture of iron solids with different oxidation states is obtained at the end of the reduction period (a molar composition of the bed equal to 0.01/0.80/0.19 can be calculated for Fe_3O_4/FeO/Fe, respectively, based on equilibrium calculations [35]), which have lower oxygen carrying capacity than pure Fe particles (0.136 vs 0.30 kg O_2/kg Fe_2O_3, see Table 1). On the contrary, no intermediate iron oxide species (Fe_3O_4, FeO) are considered in the reactor reference design of Case B where complete reduction of Fe_2O_3 to Fe and full H_2 conversion are assumed during charging stages, which can be achieved by condensing out the water at reactor exit and recycling back unconverted H_2. Finally, the use of Nickel-based solids as oxygen carrier is assessed in Case A.2 as an alternative to iron solids, since full CH_4 conversion can be virtually achieved when NiO reduces back to Ni in the reactor [42].

Further assumptions are reported in Table 1. The volume fraction of active oxygen carrier in the bed is taken to be 0.3 in all cases to account for any volume change due to oxidation and/or the possibility of using an oxygen carrier support. The minimum gas temperature at reactor inlet has been set at a conservative value of 550 °C to ensure fast intrinsic oxidation kinetics, as assumed in equation (1). Lower values could be considered when highly reactive solids (e.g. Copper- or Nickel-based oxygen carriers that oxidize quickly at moderately low temperatures) are used in the first section of the reactor. Moreover, the gas velocity at the inlet of the gas conduits is fixed at 25 m/s, whereas the inlet gas pressure is 5 atm[1]. It is important to highlight that these values, used as reference for reactor design purposes, correspond to the initial inlet conditions. However, the boundary conditions of the reactor during operation will change with time as a result of the progress in the oxidation reaction and the integration in the power cycle, as discussed below. Moreover, the maximum discharge time selected for the reactor is 4 h at reference conditions.

In the calculated case A.1/A.2/B reactor designs, solids are arranged into thin layers of 0.028/0.017/0.015 m located in between 51/58/60 flat gas conduits of 0.016 m height, which have 0.001 m thick perforated walls with a fraction of wall occupied by orifices/pores of 0.06 (see results in Table 1). The reactors have a square cross section between 3.8 and 5.3 m^2 and lengths from 15 to 29 m, whilst the pressure drop is below 5% in all cases. The energy storage capacity of the reactors is 125 MWh_{th}. As can be seen in Table 1, large differences are found in the energy density of the reactors due to the different oxygen carrying capacity of the particles. An energy density of 2214 kWh_{th}/m^3 can be achieved with Fe/Fe_2O_3 solids in case B, since these particles have high volumetric oxygen carrying capacity (see Table 1), whereas it is equal to 1474 kWh_{th}/m^3 in case A.2 using Ni/NiO. The lowest energy density is found for the Fe_3O_4/FeO/Fe mixture in case A.1, taking a value of 816 kWh_{th}/m^3. All reactors are rated at a maximum power of 50 MW_{th} at full state of charge (SOC), however, it reduces down to 22 MW_{th} at minimum SOC after 4 h of operation for reference flow inlet conditions ($T_{gas,in}$, $m_{gas,in}$ and $x_{O2,in}$ in Table 1), whilst the gas discharging temperature ranges from ~ 1000 °C (SOC = 100%) to ~ 752 °C (SOC = 0%) operating them with fixed air mass flow rate and in the absence of any thermal recuperative strategy.

These preliminary designs represent a trade-off between high energy density in the reactors - desired from an energy storage perspective-, and steady and limited thermal power decay during discharge, which facilitates integration of the reactor in the power cycle. Alternative more compact reactor designs with higher energy density are possible if a thicker solids bed is placed in between gas conduits. However, this comes at the expense of a more pronounced decay in the thermal power output with time, due to the larger resistance towards oxygen diffusion as the reaction front moves deeper in the bed of solids (see equation (2)). On the contrary, a softer power decay would take place if shallower solids beds were to surround the gas conducts, which would entail a reduction in the energy density of the device.

2.3. Power decay curve definition

In order to reduce the computational effort due to the power cycle optimization procedure, the behavior of the reactors during discharge (which is the same in all investigated cases, as discussed in section 2.2) is implemented in the power plant cycle model by adopting a reduced order analytical model function of gaseous (air) stream inlet conditions and reactor SOC. To this end, the reactors performance has been calibrated through eight different discharge numerical tests considering changes for the inlet mass flow rate $m_{gas,in}$ (+20%, −50%) with respect to reference value of 100 kg/s, inlet oxygen molar fraction $x_{O2,in}$ (-6%, −4%, −2%) with respect to reference value (21%) and the reactor inlet temperature $T_{gas,in}$ (500 °C, 600 °C, 750 °C) with respect to the nominal

[1] The latter value has been chosen according to a preliminary analysis of the power cycle optimal parameters.

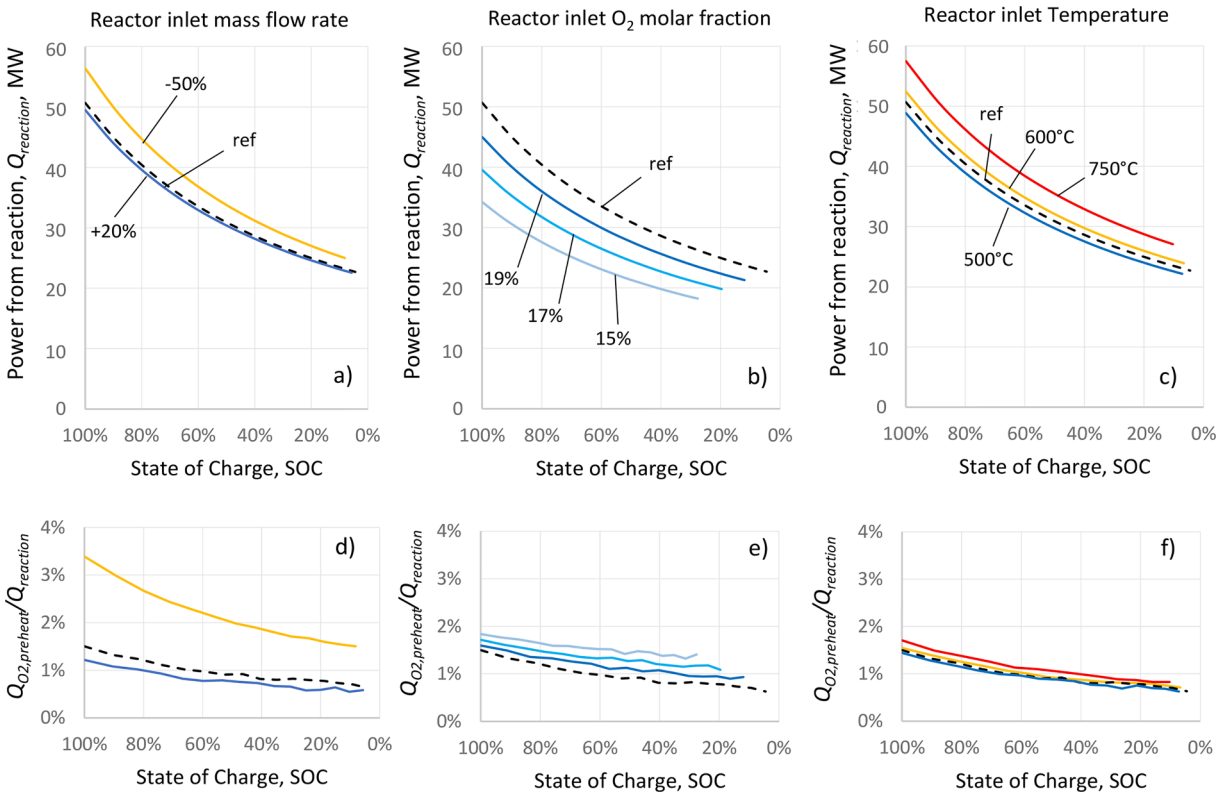

Fig. 4. (top) Thermal power released from oxidization of the metallic material: Power decay curves for 4 h of discharge of the reference reactors in cases A.1, A.2 and B, (bottom) ratio between the power required for internal oxygen preheating with respect to the power generated by reaction, while changing the inlet stream parameters ($m_{gas,in}$ (a, d), $x_{O2,in}$ (b, e) and $T_{gas,in}$ (c, f),).

value (550 °C), while all the other parameters remain unchanged (results are depicted in Fig. 4).[2]

Specifically two analytical functions have been calibrated as function of the operating conditions. The first one refers to the whole oxidation power ($Q_{reaction}$) (see Fig. 4.a-b-c) which is used to calculate the mass flow rate of reacted oxygen that diffuses through the permeable gas conduit wall and thus to calculate the gas composition at reactor outlet. The second one is the power fraction that is used to heat up the gases (Q_{gas}) leaving the reactor, which is slightly lower than the whole oxidation power because a small fraction is used to preheat the diffusion oxygen ($Q_{O2preheat}$) that reacts with the oxygen carrier along the reactor (see Fig. 4.d-e-f). Results show that the oxygen content in the inlet gas flow is the variable that affects the reaction power the most: the lower the oxygen content, the lower the released power at the same SOC level, thus resulting in an increase of discharge time (or a higher final SOC for the same discharge time as depicted in Fig. 4.b-e). Nevertheless, moderate changes in the inlet flow rate and temperature of the gas have a limited effect on the reactor heat output. The results obtained from the discharge simulation tests reported in Fig. 4 have been interpolated with a multiparameter analytical function that represents the trend of $Q_{reaction}$ and Q_{gas} as function of the initial SOC, inlet gas temperature, inlet mass flow rate and oxygen fraction to the reactor (SOC, $T_{gas,in}$, $m_{gas,in}$ and $x_{O2,in}$, respectively). This function has been obtained by means of the Ordinary Least Squares (OLS) method with GRETL [43] starting with a very large number of independent terms (logarithmic and polynomial terms of each single variable as well cross terms of different variables) and adopting a sequential method in order to eliminate less representative ones. The final selected form is a pure numerical representation of numerical data with an adjusted R^2 equal to 0.999998% and requiring 24 terms, as reported in Table A.1 in the annex section A.I. It is important to note that the obtained reactor designs and above considerations on the power decay curve can be virtually scaled up or down linearly (variation of frontal area and distribution of channels) to account for reactors of different size.

3. Power plant modelling and optimization tool

A numerical Matlab tool [44] as been developed to (i) calculate the performance of the system under nominal and off design conditions, (ii) perform the optimization of the cycle design for the single reactor system and (iii) evaluate the system performance over a complete discharge in both single reactor and multireactor configurations. The following subsections detail the strategies and main assumptions of the numerical model.

3.1. Power cycle configurations, main assumptions and off-design modelling

The reactors designed above are used to replace the combustor in an open Brayton cycle. The simplest configuration given by an open gas cycle (non-recuperative) is ruled out as an option for this application under the selected boundary conditions. In this configuration, the reactor inlet temperature would decrease in part load operation, involving very high pressure ratios in order to reach the target of minimum reactor inlet temperature ($T_{gas,in}$) value (550 °C, see Table 1) even at minimum load (minimum SOC) and thus, leading to an efficiency

[2] The effect of inlet gas pressure has not been considered in this analysis, as the oxygen flux through the orifices of the gas conduit walls and thus, the reactor performance, is independent of pressure. This is because the oxygen diffusion flux is assumed to follow Fick's law and therefore, it is directly proportional to the product of oxygen diffusivity and concentration gradient (see equation (1)). These variables are inversely and directly proportional to pressure, respectively, hence cancelling the effect of pressure on the oxygen diffusion and the thermal power release in the reactor.

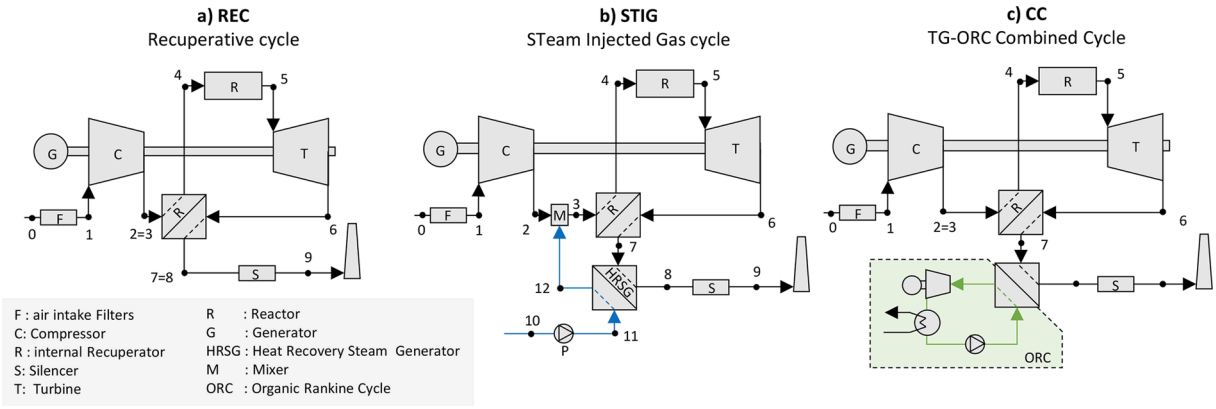

Fig. 5. Plant schemes for the three cycle configurations investigated in this work.

Table 2
Assumptions adopted for the design of the power plant.

Pressure drops	
Filter	1%
Recuperator hot and cold side	3%
Reactor	5%
HRSG hot side	1%
HRSG cold side	5%
Silencer	1%
Nominal efficiency	
Compressor	0.88
Expander	0.9
Pump	0.85
Gearbox	0.97
Generator	0.98
ORC second law	0.55
Temperatures constraints	
Minimum ambient temperature, °C	20
Minimum reactor inlet temperature, $T_{gas,in,\ min}$, °C	550

penalization and issues on compressor operability. This cycle configuration could, however, be an option when metallic materials allowing for a lower reactor inlet temperature are adopted as discussed above. In this work, the recuperative (REC) open power cycle shown in Fig. 5.a is taken as reference, since the use of a recuperator allows to preheat the compressed air and meet the reactor inlet temperature constraint at any load and SOC. In addition, optimal pressure ratio is low (around 5) leading to a more compact design of turbomachinery. The maximum reactor outlet temperature is ∼ 1000 °C and therefore, uncooled expansion is considered assuming the adoption of non-conventional materials for first turbine rows as ceramic matrix composites that can withstand temperatures up to 1200 °C without internal or film cooling solutions [45]. Additionally, the lack of turbine blade cooling allows to use a recuperator with very similar hot and cold side heat capacities (differences are due to a small consumption of oxygen in the reactor and consequent little variation of both mass flow rate and specific heat) and thus, with very uniform temperature difference, and more pronounced exhaust cooling with respect to conventional cooled expansion recuperative cycle. In spite of this peculiarity, a consistent amount of heat is still available for heat recovery at recuperator outlet. In order to exploit this available heat, two additional cycle configurations are analyzed. The first one is a STeam Injected Gas turbine (STIG) cycle (see Fig. 5.b) where the residual heat is used to generate saturated steam at cycle maximum pressure, which is then mixed with compressed air at compressor outlet. This configuration is characterized by a lower oxygen content in the gas at reactor inlet and thus, a lower thermal power released by the reactor and longer discharge time. Water is required, with a consequent pump consumption, but the higher overall mass flow rate in expansion with respect to the mass flow rate compression leads to a positive impact on cycle performance. The third configuration shown in Fig. 5.c is a combined cycle (CC) configuration where the bottom unit is designed as an Organic Rankine Cycle (ORC) instead of a steam cycle according to the low temperature at recuperator outlet and the small available power output: a configuration that is largely adopted in natural gas compression stations [46]. In this case, the impact on the performance of the gas cycle will be limited to the introduction of an additional pressure drop at turbine discharge, but the amount of electrical power output from the ORC overcomes this penalization.

The three cycle configurations have been simulated and optimized considering the assumptions reported in Table 2 for the design of the components. The global heat transfer coefficients for the recuperator and steam generator are calculated assuming finned tube heat exchangers and considering heat transfer coefficients equal to 125, 2000 and 5000 W/m^{2}K for gas flow, liquid water and water in phase transition, respectively[3]. Fouling resistance coefficients are considered equal to $1.8{\cdot}10^{-4}$ and $1.5{\cdot}10^{-3}$ m^{2}K/W for gas and water sides, respectively, and external to internal area ratio is assumed equal to 5 for finned tubes in the recuperator and the HRSG. Fluid thermodynamic properties have been calculated using Refprop database [47] in order to properly account for the water content in the STIG configuration.

In order to analyze the plant performance during a reactor discharge, the off-design performance of the different plant components represented in Fig. 5 is numerically described as follows:

- **Turbomachinery**. The power system performance and operability is strongly affected by the turbine-compressor shaft off-design behavior. For large-scale systems, the use of constant speed (CS) shaft at 3000 RPM (3600 RPM for countries with 60 Hz grid) is the most appropriate solution because of the difficulties to design and operate large variable speed gearboxes or large power electronics. In this case, the compressor is generally provided with variable inlet guide vanes (VIGV) in order to vary air volumetric flow rate at compressor intake and provide the system by a larger operability range. Differently, for small-scale systems, a variable speed (VS) shaft connected to a power electronic system for output frequency control can be used to allow a wider operative range. In some cases both features are installed in order to provide a better control of the system especially during transients. The operative maps of the two reference compressors with efficiency information are derived from literature [48–50] and reported in Fig. 10.c-d: VS shaft can change the rotational speed in the range between −15.5% and + 3% while

[3] Effect of gas pressure has been neglected considering the low pressure ratio of the optimized power plants.

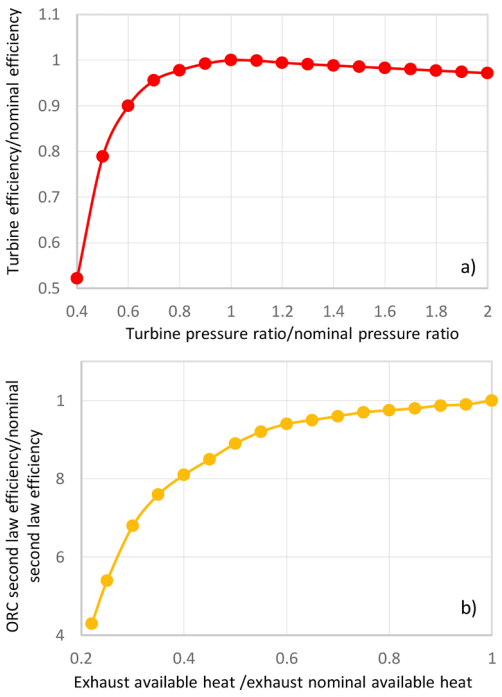

Fig. 6. A) Dimensionless turbine performance curve against pressure ratio, b) dimensionless ORC performance curve against available thermal input.

VIGV angle can be varied between −10° and 40°; the minimum efficiency in the operative map is around 90% for both compressor type, with respect to the nominal efficiency. The turbine has been assumed to work always in choked conditions with a constant reduced mass flow rate (see equation (6)) independently of the rotational speed and so the same function is adopted for both CS and VS cases.

$$m_{r,T} = \frac{m_{in,T}\sqrt{T_{in,T}}}{p_{in,T}} \tag{6}$$

where $m_{r,T}$ is reduced mass flow rate at turbine inlet, $m_{in,T}$ is the actual mass flow rate at turbine inlet (kg/s), and $T_{in,T}$ and $p_{in,T}$ are turbine inlet temperature (K) and pressure (bar), respectively. Fig. 6.a depicts the dimensionless expander performance curve as function of beta as derived from [51].

- **Heat exchangers.** The heat transfer coefficients and pressure drops in a heat exchanger vary on both hot and cold sides when working under off-design conditions, whilst the heat transfer area is constant. These are calculated using equation (7), which shows that heat transfer coefficients are proportional to the mass flow rate power 0.8 according to forced convection heat transfer coefficient definition [52], while pressure drops are proportional to the mass flow rate power 1.86 [51]:

$$X_{offD} = X_{onD}\left(\frac{m_{offD}}{m_{onD}}\right)^{\alpha}\begin{cases} if X = h; \alpha = 0.8 \\ if X = \Delta p; \alpha = 1.86 \end{cases} \tag{7}$$

where X_{offD} and X_{onD} represent the calculated quantity, heat transfer coefficient (h) or pressure drop (Δp), in off-design and design conditions respectively, m_{offD} and m_{onD} are the fluid mass flow rates in off-design and nominal conditions respectively, α is the exponential coefficient. Area of the recuperator is evaluated adopting a discretized method based on 20 nodes in order to correctly evaluate the local temperature difference.
- **Reactor.** To limit computational effort, integration of the reactor off-design performance into the power plant analysis is carried out by means of the analytical equations ($Q_{reaction}$ and Q_{gas}) calibrated on the sensitivity analysis results presented in Section 2 as function of gas inlet temperature, mass flow rate, oxygen molar fraction and reactor SOC. The pressure drops in the reactor at different operating conditions are obtained using equation (7).
- **Organic Rankine Cycle.** The ORC power output in the system of Fig. 5.c is calculated with a simplified approach multiplying the reversible power available from the hot gases released by the gas turbine recuperator (namely the gas stream flow exergy with respect to ambient condition) by a second law efficiency. This last parameter is not constant during off-design conditions and is varied as a function of the available thermal power in the gas stream to account for the inevitable penalization arising from the off-design operation of the ORC turbine. The adopted off-design performance curve is derived by [53] and reported in Fig. 6.b.
- **Other components.** The filter and silencer pressure drops are corrected in off-design scenarios from nominal value in Table 2 according to equation (7).

Once the cycle design is selected (nominal turbomachinery mass flow rate and pressure ratio, heat exchanger size), the calculation of the operative point for a given energy storage released thermal power requires an iterative numerical procedure to solve the off-design problem while keeping constant the turbine inlet temperature at 1000 °C (i.e. the reactor outlet temperature). To this end, a numerical Matlab tool that incorporates the above considerations has been developed. In this tool, three closing variables are adopted for the recuperative and the combined cycles: air mass flow rate at compressor inlet (m_{air}), compressor pressure ratio (β_C) and reactor inlet temperature ($T_{gas,in}$). These are iteratively varied in order to minimize the relative error (closing constraints) between calculated and nominal value for three quantities: recuperator heat transfer area (A_{REC}), reactor inlet mass flow rate ($m_{gas,in}$) and turbine reduced mass flow rate ($m_{r,T}$). For the STIG case, the steam mass flow rate (m_{vap}) is added as closing variable and the error on steam generator area (A_{HRSG}) is added to the off-design problem closing constraints. The detailed scheme describing the iterative solving process can be found in Fig. A.2 in the Annex section A.II.

3.2. Single reactor configuration: Optimization of the power cycle design

The definition of the optimal power system design must necessarily take into account how the system is expected to be operated. In this particular application, the system should not be optimized for a specific operating point (for example the maximum or the minimum reactor SOC condition) because the design must consider the actual system performance during the whole reactor discharge and the operative limits of the components. For this reason, it is more appropriate to select different combinations of components design parameters and then test the resulting systems over a full discharge operation in order to find the optimal solution. The optimization process aims to maximize the energy output during a reactor discharge as outlined in equation (8). In this equation, the net electric energy output (E_{el}) accounts for the electric energy output of the gas turbine cycle ($E_{el\ TG}$), the ORC cycle ($E_{el\ ORC}$) in the combined cycle configuration (see Fig. 5.c) and the water pump consumption ($E_{el\ pump}$) associated to the STIG configuration (see Fig. 5. b). This figure of merit has been preferred to the discharge efficiency (e.g the ratio between the energy output and the actual energy discharged from the reactor) because the adoption of this latter one may lead to the definition of cycle configurations not able to maximize energy storage utilization and to minimize final SOC of the reactor with a consequent decrease of actual energy density and increase of reactor specific cost.

$$\max(E_{el}); E_{el} = E_{elTG} + E_{elORC} - E_{elpump} = \sum_{SOCmax}^{SOCmin}\left(W_{elTG} + W_{elORC} - W_{elpump}\right)\cdot\Delta t_{\Delta SOC} \tag{8}$$

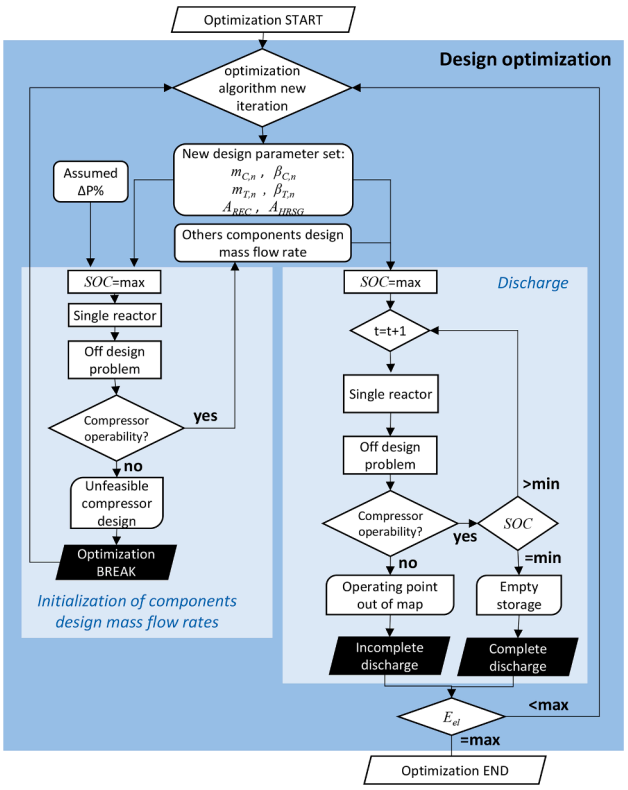

Fig. 7. Block diagram of the design optimization routine.

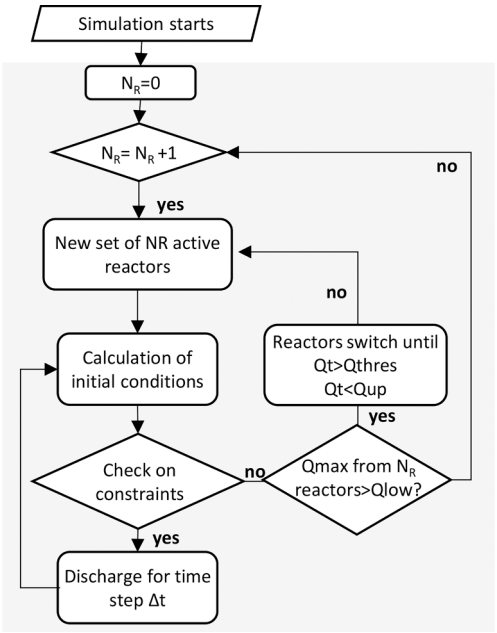

Fig. 8. Block diagram of the multireactor heuristic strategy.

where $W_{el\ TG}$, $W_{el\ ORC}$ and $W_{el\ pump}$ are the electrical power produced by the gas turbine cycle and the ORC and consumed by the water pump, respectively in time step Δt associated to a given ΔSOC of discharge.

Fig. 7 depicts the flow diagram of the Matlab optimization numerical routine followed in this work, which is designed to find the optimal plant design that provides the maximum value of the electrical energy output using different combinations of the following design parameters:

- Compressor nominal intake air mass flow rate and nominal pressure ratio ($m_{C,n}$, $\beta_{C,n}$). These parameters are used to scale the nondimensional compressor map in order to account for a realistic compressor efficiency during discharge.
- Turbine nominal inlet mass flow rate and nominal expansion pressure ratio ($m_{T,n}$, $\beta_{T,n}$). These parameters are used to scale the normalized turbine curve and to determine the nominal turbine reduced mass flow rate value for a fixed maximum cycle temperature (equivalent to the maximum reactor outlet temperature, which is taken to be 1000 °C in this work to prevent from any agglomeration or sintering of the oxygen carrier that may compromise its stability over cycles).
- Recuperator heat transfer area (A_{REC}). This parameter affects the temperature at combustor inlet and the available power for water evaporation (STIG configuration) and in the ORC cycle (CC configuration).
- Heat recovery steam generator heat transfer area (A_{HRSG}). This parameter is present only in the STIG configuration and affects the steam mass flow rate production.

Each single design defined by a combination of variable design parameters (5 for REC and CC configurations, and 6 for the STIG cycle) is first tested at maximum SOC in order to verify the system operability and calculate the reference mass flow rate for pressure drops[4]. In case of positive check, the system is then simulated from reactor full SOC to the minimum operating point. The latter can coincide with SOC ~ 0 or it may involve a final SOC greater than 0 because of the limit of compressor operability at low volume flow rates, thus hindering full reactor discharge. Each operating condition requires the resolution of the off-design problem shown in Fig. A.2 in the Annex section A.II. The optimization problem is constrained by two additional conditions: (i) the maximum computed pinch point temperature difference in the recuperator and HRSG must be higher than 30 °C and 15 °C, respectively (otherwise, recuperator and HRSG size would be pushed towards infinite values by the optimization algorithm due to the positive effect on the cycle performance) and (ii) the minimum temperature at the reactor inlet during discharge is fixed at 550 °C, as explained in Section 3.1. The optimization procedure ends when the electrical energy output is maximized for a set of variable design parameters. During reactor discharge, a SOC step equal to 3% is adopted. P*atternsearch* algorithm has been selected for the resolution of the off-design problem: this algorithm evaluates, at each iteration step, the objective function over an increasing/decreasing/rotating mesh of tentative solution without requiring gradient calculation [54]. As result, it is able to handle non-continuous and non-differentiable functions and to avoid local minimum/maximum. This algorithm has been preferred to simple *fmincon* and complex *genetic* or *particle swarm* algorithms because it shows a good compromise between computational time and accuracy of the solution.

3.3. Analysis of the multireactor configuration

The use of a multireactor configuration with several reactors in parallel is investigated to enhance the flexibility of the system. In this scheme, different reactors switch between active or inactive mode at different times during discharge, either to supply a rather constant thermal input to the cycle or to allow the power output to be varied with limited efficiency penalty. Finding the optimal energy storage configu-

[4] The reference mass flow rate values used to estimate the pressure drops through the compressor filter house, the silencer and the heat exchangers are calculated at the beginning of the discharge process when these parameters are at maximum value and thus, they are not selected as optimization variables. Otherwise, the optimization algorithm tends to push them towards very high and unreasonable values in order to reduce the computed pressure drops and maximize cycle efficiency.

ration sequence (i.e. definition of active/inactive reactors, namely the energy storage configuration, vs time) is an extremely complex numerical problem (see for example the MILP method developed/employed in chemical sector [55]). This is considered out of the scope of this work, which aims at providing a preliminary analysis on the feasibility and flexibility of the proposed multireactor system. To this end, an alternative method that defines the reactor management sequence for energy discharge based on heuristic strategies is employed, making use of simple rules that can be easily implemented in real systems. Fig. 8 shows the implemented strategy, which requires three power levels to be defined: Q_{low} and Q_{up}, which are the minimum and upper bounds where the power output is to be maintained, respectively, and Q_{thres}, which is the minimum total thermal power that the new configuration of active reactors shall provide after a configuration switch. Those power levels can be constant during discharge in order to keep the system power output in a relatively narrow range as demonstrated in this paper or they can be varied along the system discharge following a desired power plan. The routine starts selecting randomly a multireactor configuration able to provide a total thermal power between Q_{low} and Q_{up}. This configuration, defined by a certain number (NR) of reactors in operation, is kept unvaried if the following three constraints are verified:

- The total thermal power released at time t (Q_t) is greater than Q_{low}.
- Each reactor i in operation has a $SOC_{i,t}$ at time t higher than the average reactors SOC ($\bar{SOC}_t$) minus a certain ΔSOC.
- Each reactor i on hold at time t has a $SOC_{i,t}$ lower than the average reactors SOC ($\bar{SOC}_t$) plus ΔSOC.

The first constraint aims at keeping the total thermal power above a certain value but it may lead to a non-homogeneous depletion of the reactors, thus limiting the minimum final overall SOC and resulting in a lower equivalent energy density. The other two constraints aim at solve this issue by forcing a uniform and progressive discharge of all reactors. If one, or more, of the previous constraints is not verified, the reactors configuration is modified by progressively switching off the reactors in operation with the lowest SOC and switching on the reactors on hold with the highest SOC, thus keeping unchanged the number of reactors in operation. The process is repeated until (Q_t) is greater than Q_{thres} but lower than Q_{up}. If there is not a combination of NR reactors able to provide Q_{thres}, the number of reactors in operation is increased by one and the process is repeated.

From a rigorous numerical perspective, the design of the power system should be optimized for the specific multireactor case discharge process, namely the desired power output or power profile. However, preliminary analyses made for the recuperative (REC) cycle using both CS and VS shaft show that almost negligible performance improvement is observed if the power plant is designed specifically for the multireactor case rather than adopting the optimal design parameters calculated for single reactor case (the increase in the energy output is below 1%). In addition, the use of a power system optimized for single reactor case ensures the highest flexibility in terms of operative ramp up/down power range. Therefore, no design optimization is performed for the multireactor configurations investigated in this work, which use the optimal design parameters calculated for the single reactor case as reference (see Section 5.1) to ensure large flexibility with minor efficiency penalization.

4. Thermodynamic results and discussion

4.1. Single reactor configuration

Variable speed (VS) shaft

The results of the optimized REC, STIG and CC plant configurations that make use of a VS shaft are summarized in Table 3. All the power cycle designs analyzed allow for complete reactor discharge down to SOC close to 0% (1% in this case due to the choice of SOC step equal to 3% during discharge) and the calculated optimal parameters are rather similar in all cases. The calculated optimal cycles work at a pressure ratio lower than 5, which allows designing compact machines with few axial stages or even with a single radial stage in case of small-scale applications. Fig. 9 depicts the changes in the main operating variables as the reactor SOC reduces during discharge for the three optimal VS shaft

Table 3
Optimal results for single reactor case for the three cycle configurations adopting VS shaft and REC configurations adopting CS shaft. When two values are reported, the first refers to maximum SOC and the second to minimum SOC (beginning and end of the discharge operation, respectively).

	VS shaft			CS shaft
	REC	**STIG**	**CC**	**REC**
Optimal design parameters				
Compressor design mass flow rate ($m_{C,n}$), kg/s	125.1	109.8	123.2	116.6
Compressor nominal pressure ratio ($\beta_{C,n}$)	4.42	4.45	4.42	4.06
Turbine design mass flow rate ($m_{T,n}$), kg/s	87.32	82.34	91.77	100.1
Turbine nominal pressure ratio ($\beta_{T,n}$)	2.83	3.1	3.01	3.52
Recuperator area (A_{REC}), m^2	22,196	19,167	21,986	21,347
HRSG area (A_{HRSG}), m^2	–	487	–	–
Discharge results (for one cycle)				
Reaction thermal power ($Q_{reaction}$), MW_{th}	51.3–25.7	49.0–25.2	51.2–25.7	51.1–35.7
Minimum SOC, %	1%	1%	1%	59%
Overall electric power output (W_{el}), MW_{el}	21.2–11.5	20.9–11.4	24.5–12.4	21.5–15.3
Water pump power ($W_{el\ pump}$), kW_{el}	–	0.5–0.17	–	–
ORC power output ($W_{el\ ORC}$), MW_{el}	–	–	3.31–0.97	–
Gas cycle energy output ($E_{el\ TG}$), MWh_{el}	54.17	55.41	53.99	47.95
Water pump energy consumption ($E_{el\ pump}$), kWh_{el}	–	0.18	–	–
ORC energy output ($E_{el\ ORC}$), MWh_{el}	–	–	5.9	–
Overall net energy output (E_{el}), MWh_{el}	54.17	55.41	59.99	47.95
Average net electric efficiency, %	44.3%	45.3%	48.9%	43.1%
Discharge time, h	3.56	3.65	3.57	1.32
Air mass flow (m_{air}), kg/s	126.1–81.8	111.7–75.8	125.3–81.6	122.5–96.9
Water mass flow (m_{vap}), kg/s	–	3.37–0.75	–	–
Compression pressure ratio	4.37–2.71	4.53–2.87	4.40–2.74	4.44–3.41
Hot side Recuperator outlet temperature, °C	219–163	222–169	220–164	221–194
Reactor inlet temperature ($T_{gas,\ in}$), °C	645–729	643–719	644–728	636–681
Total water consumption, kg	–	19,954	–	–

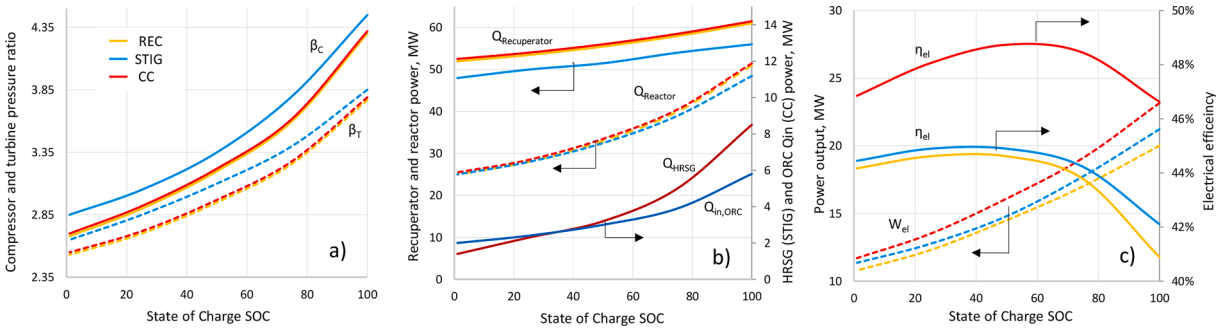

Fig. 9. Results for the three different cycle configurations and VS shaft for single reactor case. a) compressor and turbine pressure ratio, b) Thermal power at the reactor, recuperator, HRSG and heat available for the ORC, c) overall power output and cycle efficiency.

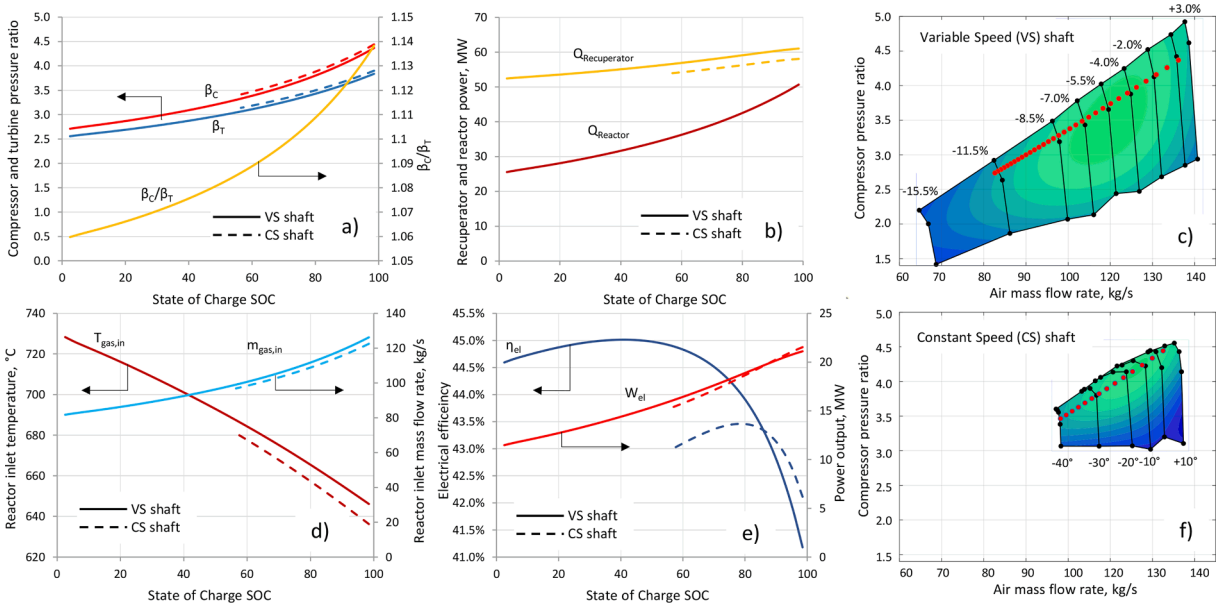

Fig. 10. Comparison between REC configuration adopting a VS shaft (top figures) and a CS shaft (bottom figures. a) turbomachinery pressure ratio, b) recuperator and reactor thermal power, c) operative points on the compressor map for the VS case, d) reactor gas inlet temperature and inlet mass flow rate, e) power and efficiency trend, f) operative points on the compressor map for the CS case.

configurations analyzed, while Fig. 10 adds more information on other cycle parameters only for the REC configuration. Similar trends are found in all cases, with a close overlap between the REC and the CC configurations for most of the quantities, since the two plants differ only in the presence of the ORC that is bottomed to the main gas cycle. Both the compressor and turbine pressure ratios reduce during discharge (Fig. 9.a), whereas the β_T/β_C ratio increases due to the reduction in the pressure drops (Fig. 10.a). It is possible to note that optimization algorithm selects a turbine nominal pressure ratio that is generally lower than the actual one during the discharge, in agreement with the implemented off design performance curve of the turbine which is more penalized for pressure ratios lower than the nominal (see Fig. 6.a). The recuperator heat duty is always larger than the reactor duty and is more stable for the whole SOC range (see Fig. 9.b), because at reduced load the reduction of air mass flow rate at compressor intake (Fig. 10.d) is balanced by a higher maximum enthalpy difference between cold and hot stream (the turbine outlet temperature increases while the compressor outlet temperature reduces as a consequence of pressure ratio reduction). Considering the reduction in the global heat transfer coefficient during discharge, the recuperator pinch point slightly increases during discharge and reaches the 30 °C constraint at minimum SOC while the reactor inlet temperature increases from nominal point (645 °C) to over 720 °C as effect of turbine outlet temperature increase (Fig. 10.d). As expected, the thermal power supplied by the reactor strongly reduces as the reactor SOC diminishes, and nearly halves at minimum SOC (see Fig. 9.b and Fig. 10.b).

Main differences of the STIG configuration with respect to the REC cycle are: (i) the higher pressure ratio of the STIG cycle that also causes a lower recuperator duty, (ii) the lower thermal power released by the reactor because of the effect of the lower reactor inlet temperature and a lower oxygen content at the reactor inlet, (iii) the higher power output thanks to the increased mass flow rate in expansion although the steam to air ratio is always relatively low (around 3% at full SOC and 0.5% at minimum SOC according to the stronger reduction of the duty available at HRSG as reported in Fig. 9.b), (iv) the slightly higher efficiency (max + 1%). Regarding CC configuration it can be noted that the optimal design parameters are very similar to the REC case since it is not convenient to penalize the top cycle (GT) efficiency in order to increase the flue gas stack temperatures and then increase the power output and the efficiency of ORC. This is due to the larger power output and efficiency of the gas turbine with respect to the ORC and the limitation of ORC in exploiting high temperature heat sources due to thermochemical stability limit of organic fluids[56]. Thermal power available for the ORC decreases (see Fig. 9.b) during discharge causing an ORC power production that ranges between 3.1 MW at maximum SOC and 0.9 MW at minim SOC. The ORC power output contributes to a consistent

Table 4
Results for the sensitivity analysis related to Q_{thres} and ΔSOC parameters for the REC configuration with CS shaft. Combination of Q_{thres} equal to 47 MW and ΔSOC equal to 5% results in a non-feasible system operation.

Q_{thres}, MW_{th}	45				46				47			
ΔSOC, %	∞	15	10	5	∞	15	10	5	∞	15	10	5
Average electric power, MW_{el}	19.4	19.8	19.9	20.1	19.4	19.9	20.1	20.2	19.6	20.1	20.2	–
Average thermal power, MW_{th}	46.4	47.2	47.7	48.0	46.5	47.7	48.1	48.3	47.0	48.0	48.4	–
Average net electric efficiency, %	41.82	41.8	41.85	41.84	41.79	41.79	41.81	41.81	41.79	41.8	41.77	–
Number of reactor switches during discharge	26	27	28	36	18	21	20	26	14	15	17	–
Minimum single reactor SOC at the end of discharge ($SOC_{end,min}$), %	14.9	9.2	6.7	6.2	16.2	9.5	6.7	5.5	15.0	8.4	7.7	–
Maximum single reactor SOC at the end of discharge ($SOC_{end,max}$), %	44.9	23.1	15.3	10.6	47.1	22.9	14.7	9.3	41.3	21.8	16.0	–

efficiency increase between + 5 and 2.5 points of efficiency depending on the SOC level. Fig. 10.c depicts the operative map of the VS shaft compressor in REC case, where red dots represent operative points calculated with a 3% SOC discharge step for full reactor discharge from SOC 100% to SOC 1%. Compressor operation starts close to the map upper bound at maximum SOC and then moves towards lower mass flow rates during reactor discharge according to reactor power decay curve. Pressure ratio is reduced as well according to the sliding pressure operation of the turbine and therefore, the compressor always operates in the maximum efficiency region sufficiently far from the surge line.

As can be seen in Fig. 9.c, net electric efficiencies between 41% and 49% can be achieved for all cycle configurations, with only small variations (around 2 net points) throughout discharge despite the marked decrease in the power output. In all cases, the cycle efficiency increases at the beginning of the discharge as a result of the higher compressor efficiency, the progressive reduction of the cycle pressure drops and the higher heat exchangers effectiveness. After reaching a maximum, the efficiency slightly decreases mainly because turbomachinery performance decay. Maximum in efficiency is different for the different plant configurations adopting VS shaft. For the REC and STIG cycles, the optimum takes place with a heat input equal to 60% of the nominal (reactor SOC = 40%), while for the CC configuration it corresponds to around 70% of the nominal input (reactor SOC = 60%) because of the penalization of ORC performance at low loads. As shown in Fig. 9.c, the CC configuration has the highest cycle efficiency, with values between 48% and 49% during the entire discharge operation. This represents a 9% increase in the total energy output with respect to the REC configuration. On the contrary, the efficiency gain associated to the STIG cycle with respect to the REC system is limited to ~ 1%. This suggests that the use of the STIG cycle can be avoided, thus saving the HRSG investment cost, the operative cost associated to water demineralization and avoiding water consumption (estimated to be 6000 t/yr considering 300 charge and discharge cycles annually).

Constant speed (CS) shaft

Analysis of systems adopting a constant speed (CS) shaft has been also carried out for the REC configuration as summarized in Table 3 while a comparison against the REC cycle with VS shaft is reported in Fig. 10. Also in this case, full exploitation of the compressor operative map is possible (see Fig. 10.f), with first and last operative points (red dots in the figure) close to the upper and lower bound of the envelope, respectively. However, operational limits of a compressor equipped with VIGV in terms of minimum air mass flow rate involves that the reactor can only be discharged to a final reactor SOC of 60% and for a total discharge time 1.3 h making the CS shaft configuration not attractive for single reactor applications. In addition, performances are lower with a maximum performance 1.5 points of efficiency below the VS shaft case.

Remarks on the single reactor case

Despite the low complexity and high efficiency associated to this system (see Table 3), the progressive decay in the power output during discharge represents a major operating constraint. It reduces the operational flexibility of the system, leaving little possibility for control unless dissipative methods like bypassing the turbine, the HRSG in the STIG configuration or bypassing the ORC in CC configuration are used. Another option that provides full flexibility during discharge consists of burning a gaseous fuel at the reactor inlet/exit to compensate for the reduction in the reactor thermal power output, although this comes at the expense of emitting CO_2 to the atmosphere as discussed in the Introduction section. In addition, a single reactor system can be effectively exploited only adopting VS shaft machines. This is not indicated for large scale systems unless the reactor is designed for a small power decay during discharge at the expenses of energy density as explained in Section 2.2. Therefore, the single reactor configuration may not be the preferred option in future CO_2-free energy markets, where the possibility of rapidly changing the power output is key to provide grid balancing services. However, it can be an interesting solution for small systems and short-term small renewable energy storage where the produced electricity is only a fraction of the total electricity supply and grid connection ensures controllability of the system.

4.2. Multi reactor configuration

In this work, the multireactor case consists of 10 reactors in parallel, each one with an energy storage capacity of 25 MWh_{th} and a maximum thermal power of 10 MW_{th} at maximum SOC (equivalent to a reactor size equal to 20% of the previous single reactor case but with a system having a double stored capacity). The analysis is carried out at fixed minimum (ambient) and maximum (reactor outlet) cycle temperature at all discharge points (see values in Table 2), meaning that in multireactor case the mass flow rate flowing through each active reactor depends on the actual SOC of the reactor and the thermal power released as reported in Fig. A.2 in the Annex section A.II.

The multi reactor case analysis is carried out for both the REC and the CC configuration adopting CS or VS shaft. The use of STIG cycle is not considered in this case because of the limits already highlighted in the single reactor case. The two main aspects to be defined when dealing with a multireactor case are the target power and the definition of the heuristics strategies parameters in order to get a proper reactor operation and exploitation. In this study, a system operation close to maximum efficiency conditions is investigated. Therefore, Q_{low} is fixed at 45 MW and 35 MW for cycles using CS and VS shaft, respectively (see Fig. 10.e), while Q_{up} is always set 7 MW_{th} above Q_{low}. The two remaining parameters, namely the Q_{thres} and ΔSOC, have to be selected in order to ensure a proper system operation while ensuring a deep system discharge and avoiding an excessive number of reactor configuration switches. In order to assess the impact of different values on the heuristic strategy parameters, a sensitivity analysis is carried out (see Table 4) for the REC case with CS shaft by varying Q_{thres} between 45 and 47 MW (corresponding to 90 and 94% of the nominal load, respectively) and ΔSOC between 5%, 10% and 15%; in addition a case without implementing ΔSOC constraints is tested (columns with ΔSOC=∞ in Table 4) is included. As reported in Table 4, average thermal power, average power output and average electric efficiencies are relatively stable for the Q_{thres} and ΔSOC values tested, while main differences are in the number of configuration switches during discharge and the final overall SOC of the reactors involved. For multireactor systems operated only with the switching constraint related to Q_{low} (columns with

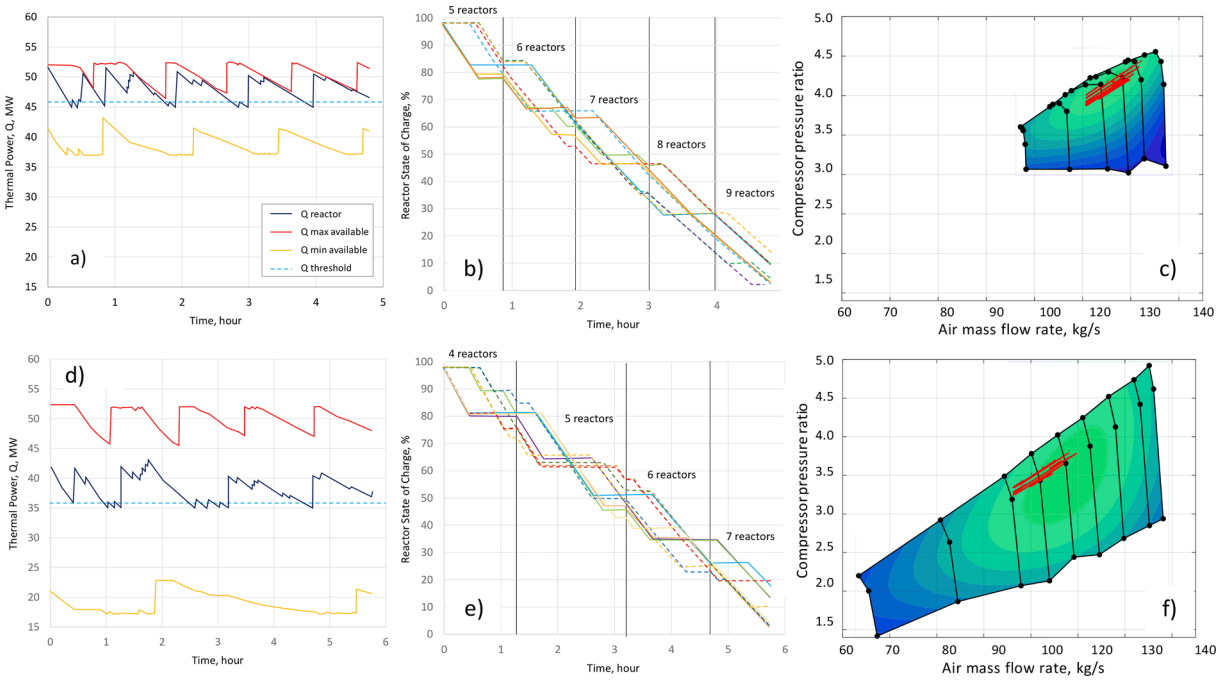

Fig. 11. Comparison between REC configuration adopting CS shaft (top figures) and VS shaft (bottom figures) in multireactor configuration. a-d) Thermal power released by the active reactors plus maximum and minimum allowable reactors overall power output at a certain time step, b-e) actual SOC of all reactors as a function of time, c-f) compressor operating points on compressor map. Results are obtained for Q_{thres}s = 46 MW_{th}, Q_{min} = 45MW_{th} and Q_{max} = 52 MW_{th} for the CS shaft case and Q_{thres} = 36 MW_{th}, Q_{min} = 35MW_{th} and Q_{max} = 42 MW_{th} for the VS shaft case. A ΔSOC = 10% is adopted in both cases.

ΔSOC=∞ in Table 4), an increase in the Q_{thres} results in drastic reduction in the number of configuration switches during discharge (i.e. from 26 to 14 when Q_{thres} increases from 45 to 47 MW), leading to much simpler management of the discharge process. However, the final reactors SOC can be very heterogeneous if the ΔSOC parameter is not tuned properly, with some reactors still having SOC greater than 40% at system discharge end. The adoption of ΔSOC = 5–15% allows to strongly reduce the final SOC of the less exploited reactors at the end of the discharge process, with final SOC values around 9% in best case. Adoption of small ΔSOC values allows to obtain a more homogeneous discharge of all the reactors as highlighted by difference in final SOC between the fullest and emptiest reactors that reduces from over 13% to below 4% when decreasing ΔSOC from 15% to 5%: this result is obtained at the expenses of the number of switches thus involving a more complex system operation.

Fig. 11 depicts more detailed results for two selected multireactor cases reporting the trend vs time of the overall thermal power released by the reactors (a, d), the operative reactors sequence (b, e) and the compressor operative points on the compressor maps (c, f). Two cases are compared, namely the REC configuration with both CS (top figures) and VS shaft (bottom figures) at optimal performance, and so, with a Q_{low} fixed at 45MW_{th} and 35 MW_{th} respectively. Main results are also reported in Table 5 where also the figures for CC configurations are reported. Both systems are able to keep the target power rather stable for the whole discharging process ensuring at the same time a proper discharging of the reactors with maximum SOC below 20% for the reactor with the larger remaining capacity. Final overall SOC is around 8% for the CS case and around 10.5% for the VS shaft case demonstrating the potential of multireactor management in getting high system depth of discharge ensuring the maximization of actual energy density. Discharging time is different for the two systems according to the different average target discharge power from the reactor but average time difference between reactor configuration switches is the same and equal to around 14 mins. Net energy output is slightly in favor of VS shaft case that is characterized by higher efficiency (as already highlighted in the single reactor case, see Fig. 10.e) in spite of the lower overall discharged energy for the reactors. Regarding the reactors management (Fig. 11.b and Fig. 11.e), it is possible to appreciate the operation of each single reactor through the whole discharge process (horizontal lines identify reactors on hold while sloped lines correspond to reactors in operation) and to highlight that the minimum number of reactors running in parallel increases from 5 (CS shaft) and 4 (VS shaft) at system maximum SOC up to 9 (CS) and 7 (VS) out of 10 at process end. Two additional lines are outlined on Fig. 11.a and Fig. 11.d, namely the maximum (red) and minimum (yellow) thermal power that could be supplied by the multireactor system at any time, just by modifying the configuration of active/inactive reactors available at that precise moment, whilst respecting system operability (i.e. compressor minimum and maximum air mass flow rate, which gives an idea of the flexibility of the system). For the CS shaft case, it is possible to increase the power output by 8.5% and to reduce it by 21.3% on average with the multireactor REC configuration, providing a moderate flexibility in the electrical supply to the grid. A more flexible discharge operation is possible when using a REC configuration with VS shaft as shown in Fig. 11.d: this system can provide a wider power range in terms of power ramp up and ramp down allowing an increase power output by 37.8% and reduce it down to 50% on average just by changes in the configuration of active/inactive reactors available at any time, while operating in the region of maximum efficiency. Fig. 11.c and Fig. 11.f shows the operating points on the compressor operative maps and it is possible to note that most of them are located in a narrow range close to compressor maximum efficiency region and that pressure ratio slightly decreases during the discharge process, since the air mass flow rate is split on a higher number of reactors in parallel leading to lower overall pressure drops.

Remarks on the multi reactor case

These results show that adoption of a multireactor system allows the system power output to be controlled by varying the configuration of active/inactive reactors throughout discharge. In these systems, a rather constant power output can be kept with only limited fluctuations during discharge. Alternatively, power output can be ramped up or down in a wide range, especially if a variable speed (VS) shaft is adopted. Moreover, the use of a multireactor solution enables to reach deep energy

Table 5
Multireactor cases results for both REC and CC configurations adopting CS and VS shaft when operated close to maximum performance.

	CS shaft		VS shaft	
	REC	CC	REC	CC
Average reactors overall thermal power, MW_{th}	48.1	48.1	38.3	38.3
Number of reactor switches during discharge	20	20	25	25
Minimum single reactor SOC at discharge end ($SOC_{end,min}$), %	6.7	6.7	10.5	9.3
Maximum single reactor SOC at discharge end ($SOC_{end,max}$), %	14.7	14.7	19.8	15.8
Average net electric power (W_{el}), MW_{el}	20.1	22.9	16.7	18.6
ORC power ($W_{el\ ORC}$), MW_{el}	–	3.28–2.54	–	2.38–1.69
Gas cycle energy output ($E_{el\ TG}$), MWh_{el}	96.33	96.02	96.21	97.33
ORC energy output ($E_{el\ ORC}$), MWh_{el}	–	13.59	–	11.52
Net energy output (E_{el}), MWh_{el}	96.33	109.61	96.21	108.85
Net electric efficiency, %	41.81	47.58	43.6	48.6
Discharge time, h	4.79	4.79	5.77	5.85
Air mass flow (m_{air}), kg/s	122.1–110.7	122.1–110.6	110.2–96.6	109.6–96.3
Compression pressure ratio	4.44–3.87	4.44–3.8	3.77–3.22	3.79–3.25
Recuperator outlet temperature, °C	222–206	222–207	198–180	198–180
Reactor inlet temperature ($T_{gas,\ in}$), °C	655–637	654–637	692–668	691–666

Table 6
General assumptions for the economic analysis.

parameter	value
Discount rate, r (%)	8
Plant lifetime, N (years)	25
Carrying Charge Factor, CCF	0.094
Number of charging/discharging cycles per year	300
Reactor charging efficiency,η_r	0.9
Balance of plant, BOP	20% of CAPEX
Total as spent cost, TASC	1.22 (CAPEX + BOP)

storage discharge in all reactors, thus maximizing utilization of the reactor capacity also in presence of a narrow compressor operative map as in CS shaft cases. Therefore, the multireactor configuration is a promising solution for both small-medium size applications and large scale systems adopting compressors provided by VIGV in CS shaft configuration. Effective reactors management requires frequent reactor switching to keep the power close to a target value, as well as a precise control of the air mass flow rate flowing through each reactor in order to reach homogeneous outlet temperatures and avoid overtemperature for operating reactors at higher SOC, which may represent a technical challenge considered the high temperatures at reactor inlet. These results, still far from a rigorous energy storage management optimization, highlight that it is possible to effectively exploit the energy available in a multireactor configuration using simple control tools.

5. Preliminary economic analysis and system layout

A preliminary economic analysis of the single and multi-reactor configurations investigated above is carried for cases A.1 and A.2 (decarbonized energy production from fuels) and case B (energy storage from renewables through hydrogen production) described in section 2.2. The selected figure of merit is the levelized cost of produced energy (LCOE), which is calculated for the different designed CLC systems by means of the following equation:

$$LCOE = \frac{\sum_{y=0}^{N}\left[\left(CAPEX_y + OPEX_y + c_{ES,y}\ E_{thC,y}\right)(1+r)^{-y}\right]}{\sum_{y=0}^{N}\left[\left(E_{elD,y}\right)(1+r)^{-y}\right]} \quad (9)$$

In the above expression, $CAPEX_y$ and $OPEX_y$ represent the annualized capital and annual operational costs at a year *y*, respectively, *r* is the discount rate, *N* is the plant lifetime, $c_{ES,y}$ is specific cost (€/MWh_{th}) of the primary energy source (i.e. the cost of fuel gas or green hydrogen for cases A.1/A.2 and B, respectively) referred to the energy stored in the reactor during the charging process ($E_{thC,y}$), and $E_{elD,y}$ stands for the electrical energy produced in the discharging process in one year of operation.

For sake of simplicity, the LCOE can be also calculated considering a reference year *y* of operation as:

$$LCOE = \left[\frac{CAPEX\ \ CCF + \bar{OPEX}_{fix,y}}{\bar{E}_{elD,y}}\right] + \left[\bar{OPEX}_{var,y} + \frac{\bar{c}_{ES}}{\bar{\eta}_{pb,y}\eta_r}\right] \quad (10)$$

In this case, CAPEX is multiplied by the Carrying Charge Factor (CCF), which represents the fraction of the capital cost to be amortized every year of operation. The adopted CCF value in this work is equal to 0.094, according to assumed values of discount rate and system lifetime shown in Table 6. This formulation of LCOE is split in two terms: the first one represents the system yearly fixed cost (including both CAPEX and average fixed OPEX costs, $\bar{OPEX}_{fix,y}$), while the second one represents the average annual variable costs due to operation and maintenance activities ($\bar{OPEX}_{var,y}$) and charging ($\bar{c}_{ES}$) [57]. In equation (10), $\bar{\eta}_{pb,y}$ is the average power block conversion efficiency, which is equal to the ratio between the electrical and the thermal energy released from the reactor in one year of operation ($E_{elD,y}$ and $E_{thD,y}$, respectively). Moreover, η_r is the reactor charging efficiency, namely the ratio between $E_{thD,y}$ and the energy stored (charged) in the reactor in one year of operation ($E_{thC,y}$). In this work, a CLC reactor charging efficiency$\eta_r = 0.9$ is assumed accounting for the heat dissipated during heating and cooling processes taking place during discharge and charge stages, respectively.

For a given CLC system having a certain CAPEX, OPEX and efficiency, the LCOE value mainly depends on the following two parameters, as highlighted in equation (10):

- Number of charging/discharging cycles per year, since this parameter directly affects the yearly electrical energy yield ($E_{elD,y}$). In this work a daily cycling operation is considered, assuming 300 charge/discharge cycles a year (system availability equal to 82%).
- The primary energy source specific cost ($\bar{c}_{ES}$), referred to the thermal energy stored in the charging process. Neglecting this latter term is equivalent to assume fuel for free (i.e. zero cost opportunity fuel in Case A). This is a very particular condition and may, therefore, lead to misleading results especially when comparing technologies that have different capital cost and round trip efficiency [57–59]. However, it is particularly interesting when discussing the use of biogas or other opportunity fuel gases, during the energy charging steps of the

Table 7
Reactor CAPEX (BOP and financial costs included) for the single reactor case and for each reactor in multireactor case.

	Single reactor case		Multireactor case	
	Cost, k€	Specific cost, €/MWh	Cost per reactor, k€	Specific cost, €/MWh
Reactor capacity, MWh_{th}	125		25	
Reactor CASE A.1 (Fe-based)	5540	44.7	1530	61.7
Reactor CASE A.2 (Ni-based)	6900	55.7	1910	76.9
Reactor CASE B (Fe-based)	2490	20.1	690	27.8

Table 8
Selected CAPEX correlations for each equipment in the analyzed system.

Component	Cost correlation in €2020	Range	Ref.
Reactor (BOP included)	$81000(V_R)^{0.8}$		
Turbine	$9174(m_{in})(\beta)^{0.5}\left(\frac{\eta}{1-\eta}\right)^{0.85}$	m_{in} = 25–455 [kg/s] β = 5–15	[63]
Compressor	$4281(m_{in})(\beta)^{0.45}\left(\frac{\eta}{1-\eta}\right)^{0.45}$	m_{in} = 25–455 [kg/s] β = 5–15	[63]
Recuperator	$996.139(A)^{0.78}$	NA, A [m^2]	[64]
HRSG	$-0.5601(A)^2 + 1315.3(A) + 207749$	A < 800 [m^2]	[71]
Water pump	$1354.98(W_{el})^{0.3}$	0.4<W_{el} < 30 [MW]	[72]
Generator	$2317(W_{el})^{0.5463}$	4–750 [MW_{el}]	[73]
ORC (BOP included)	$6370(W_{el})^{0.8}$	1–10 [MW_{el}]	[68]

Table 9
CAPEX cost breakdown for the five cycle configurations optimized in this work. VS shaft plants are used in both the single reactor and the multireactor case while CS shaft plants are adopted only for multireactor cases. Water pump cost has been calculated but not reported in table considering its almost negligible contribution in cost.

	VS shaft			CS shaft	
	REC	STIG	CC	REC	CC
Turbine, k€	8723	8609	9455	12,785	12,923
Compressor, k€	2569	2256	2523	2254	2204
Recuperator, k€	2446	2181	2428	2372	2373
Generator, k€	534	530	579	539	0
HRSG, k€	0	715	0	0	0
Water pump, k€	0	0	0	0	0
ORC (BOP inc), k€	0	0	4169	0	4169
BOP, k€	2855	2858	2997	3487	3616
Financial, k€	3768	3773	4873	4603	5690
CAPEX, k€	**20,895**	**20,924**	**27,024**	**25,528**	**31,556**
Specific cost, k€/kW_{el}	**988**	**1003**	**1103**	**1187**	**1283**

system. Assumptions related to $\bar{c_{ES}}$ calculation are reported below in Section 5.2.

5.1. CAPEX and OPEX evaluation

The total investment cost (CAPEX) of the system is obtained as the sum of each equipment cost, then multiplied by 1.2 to account for Balance of Plant (BOP) cost related to piping and instrumentation and by 1.22 in order to account for financing and other owner costs (see Table 6). In this work, the cost associated to each component is calculated adopting the following assumptions:

- **Reactor.** The specific cost of the novel CLC reactor, despite being largely uncertain at present, is assumed to be of 81 $k€_{2020}/m^3$ (including BOP), with an average scale factor of 0.8 on reactor volume (see Table 7). This value has been calculated as an average from economic data provided by two reference CLC projects that make use of pressurized packed bed CLC reactors (Ascent and Democlock, see REFs [60]). No additional costs have been considered for the iron-based oxygen carrier material (Cases A.1 and B), which is inexpensive and assumed to be included in the reactor cost (as in [61]). However, a reactor specific cost multiplier equal to 2 is applied for Case A.2 to account for the high cost of nickel solids. In the multireactor configuration, the individual reactor reference specific cost can be expected to be lower than that of a single reactor, since it would be possible to adopt a single insulated case with different separated reactor sections connected by piping to the same manifold, instead of using several separeted insulated reactors. However, the same specific cost as in the single reactor case has been assumed to take into account possible cost increases related to the more complex management of reactors discharge.

  Table 7 reports the CAPEX (BOP and financial costs included) for the reactors investigated in this paper. The calculated specific single reactor cost ranges between 20 and 56 €/MWh_{th}, with the lowest value attainable in Case B which is characterized by the higher energy density, and the highest cost corresponds to Case A.2 using a Ni-based oxygen carrier. For multireactor case, the specific cost increases by 38% according to scale economies.

- **Gas cycle and ORC plant.** Estimation of the power plant cost requires knowledge of the specific cost of each component, i.e. compressor, turbine, recuperator and generator (plus ORC for the CC configuration, and HRSG and water pump for the STIG configuration). In spite of the very common use of gas turbine cycles, cost estimations for each individual piece of equipment (mainly compressor and expander) are not widely available in the open literature because these plants are commercialized as a unique package. The choice of the compressor and expander cost correlations in this work is based on the comparison of references [62–67], as detailed in the Appendix section A.III. The selected cost correlations are summarized in Table 8, together with the cost correlation for all the other cycle components (a $\$_{2020}$ to $€_{2020}$ conversion factor equal to 0.88 is adopted). ORC cost has been derived from literature [68].

Regarding OPEX costs, the following values have been adopted: Gas cycle fixed O&M = 6.15€/kW_{el} per year, Gas cycle variable O&M = 0.6 €/MWh, ORC fixed O&M = 2% of ORC investment cost per year [69,70].

Table 9 reports the capital cost breakdown for the five cycle configurations considered in this work (cycle CAPEX is the same for both the single and multireactor options), as optimized for the single reactor case. As can be seen, capital and specific cost of REC and STIG configurations are very similar. However, the specific cost of CC configuration is around 25% larger because of the additional cost of the ORC unit. A rigorous validation of the calculated overall power plant investment cost cannot be carried out because low pressure ratio recuperative gas cycles are not a common solution for multi-MW plants. This plant configuration is generally adopted for microchp solution [74,75] with radial machines, with Mercury 50 [76] representing the unique example for large scale systems (4.6 MW multistage axial turbomachinery recuperative

turbine). Anyway, the specific cost of the REC cycle plant calculated in this work (i.e. ~ 1000 €/kW_{el}, ~800 €/kW_{el} if the recuperator cost is excluded) is around twice the reference cost for commercial gas cycles in simple cycle configuration (around 440-490€/kW_{el} [77]). This large difference is even more marked when considering that commercial turbines adopt higher pressure ratios (i.e. higher number of stages) and include the combustor and expansion cooling, thus increasing the specific cost of blades manufacturing well above that of the turbines considered in this study. Therefore, it seems that the correlations available (see Table 8) to estimate individual components cost from literature may lack in considering the effect of large scale economies and may lead to a likely overestimation of the expander cost which results around 4 times the compressor cost, as shown in Table 9. Thus, it should be highlighted that a conservative estimation of the cycle cost is performed in this work and that consistent LCOE reductions can be obtained by exploiting scale economies in the manufacturing of cycle components.

5.2. Charging cost evaluation

The specific fuel charging cost c_{ES} (second term of equation (10)) can be calculated with equation (11) for the different investigated cases.

$$c_{ES} = \frac{c_f \Delta h_{ratio}}{LHV} \tag{11}$$

where c_{ES} is expressed in €/MWh_{th} of power stored in the reactors, c_f is the cost of fuel in €/kg, LHV is the fuel lower heating value in MWh_{th}/kg. Finally, Δh_{ratio} is ratio between the LHV of the fuel and the heat of reaction of the oxidation process in the reactor, which depends on the combination of both adopted fuel and metallic oxygen carrier (0.731, 0.851 and 0.896 for cases A.1, A.2 and B, respectively).

- **Case A.** If a high H/C fuel gas is adopted as reducing gas, the products from the charging phase are primarily water and carbon dioxide when large fuel gas conversion conditions are targeted as assumed in this work. The cost of fuel has been assumed equal to 0.37 €/kg_{CH4} in case of biogas (having a content of 65%vol. CH_4 and 35% vol. CO_2) [78], while in case of natural gas a value equal to 0.35 €/kg (average price at 2020 [79]) is adopted. If CCS is implemented to obtain decarbonized electricity from natural gas or negative emissions from biofuels, an additional cost equal to 20 €/ton of CO_2 is considered accounting for both the capital cost of the CPU, the equivalent CPU electrical consumption and the CO_2 transportation and storage cost. Moreover, savings related to avoided CO_2 emissions have been considered with a carbon tax (CT) ranging from 50 €/ton to 100€/ton of emitted CO_2.

  Results for the reference case without CCS are presented in Table 10, as well as a sensitivity analysis varying the carbon tax value and the cost of natural gas by + 300% with respect to the reference value (peak price in 2022) [80]. Results for Case A are independent of system dimension and reactor overall stored energy, and are only little affected by the selected oxygen carrier, with values in the range 18.4–22.7 €/MWh (+16% using Ni in Case A.2 with respect to the use of iron in Case A.1). Adoption of CCS increases c_{ES} by around 23% and 16% in case of biofuel and methane, respectively. However, the specific fuel charging cost is remarkably reduced when including the positive effect of carbon tax, leading to close to zero c_{ES} for carbon tax of 100€/ton_{CO2} if biogas is employed for both A.1 and A.2 cases. In the case of natural gas, minimum c_{ES} is limited to 7–8 €/MWh for cases A.1 and A.2 at 2020 methane price, respectively, but rises at 62-72€/MWh if 2022 peak methane price adopting CCS and and carbon tax of 100€/ton_{CO2}.

- **Case B.** Green H_2 is used as reducing gas in this case, and Proton Exchange Membrane (PEM) electrolyzer is selected as state-of the art technology. Its electrical efficiency is assumed equal to 70% referred to H_2 LHV [59] considering that values in literature range between 60% and 80% [81–83] depending on the utilization factor. Electrolyzer specific cost depends on size and annual production rate [84]. In this work, a specific cost equal to 750 €$_{2020}$/kW_{el} (including BOP) is assumed for a 10 MW_{el} PEM electrolyzer, with an average scale factor of 0.75 [81]. Moreover, a charging cycle duration of 12 h is assumed in order to reduce PEM electrolyzer size and cost. PEM electrolyzer fixed O&M has been assumed equal to 18 €/kW per year (year 2020) and electricity cost is taken as 30 €/MWh. The equivalent calculated hydrogen price ranges between 2.7 €/kg H_2 if a full scale 10 MW electrolyzer is considered, and 3.7 €/kg H_2 if scale economies are not exploited and several modular 1 MW commercial PEM technology modules are installed in parallel. These values are in good agreement with the literature, where green H_2 costs between 2.2 and 6.6 €/kg H_2 are reported [85]. Final costs do not include incentives that can benefit the exploitation of off-peak electricity for the production of green hydrogen and/or energy storage.

  Results are summarized in Table 11. As can be seen, the stored capacity (number and size of reactors) affects the PEM dimension and thus, the cost of fuel. However, increasing the storage dimension by a factor of 4 only results in a decrease of c_{ES} equal to 11.3%. On the contrary, cost of electricity largely affects fuel cost, and a variation of + 50% reflects in a c_{ES} variation between + 26% and + 30% depending on the storage size. Considering for future years a specific cost decrease for multi-MW PEM electrolyzer down to 615 €/kW_{el} in 2030 and 330 €/kW_{el} in 2050 [86], and a reduction of OPEX down to 8 €/kWyear (year 2050), a reduction of c_{ES} is attainable in the range of –22%-26%. Finally, if scale economies are not exploited and modular 1 MW current PEM technology modules are installed in parallel, the c_{ES} value increases from + 36% up to 54% depending on the energy storage capacity.

5.3. LCOE evaluation

In order to isolate the effect of the specific fuel cost, the share of LCOE due to the equipment ($LCOE_{system}$) is first calculated for the

Table 10
Charging cost of cases A.1 and A.2: use of biofuels or natural gas.

Fuel	Biofuel		Natural gas	
Case	A.1	A.2	A.1	A.2
Oxygen Carrier	Fe	Ni	Fe	Ni
Δh_{ratio}	0.731	0.851	0.731	0.851
CO_2 emissions, kg CO_2/kg fuel	1.71		2.75	
c_{ES} ref. case without CCS (€/MWh_{th})	19.5	22.7	18.4	21.4
Relative c_{ES} variation with respect to refence case				
With CCS + no Carbon tax	+22.9%		+15.7%	
With CCS + Carbon tax 50 €/ton_{CO2}	−34.3%		−23.6%	
With CCS + Carbon tax 100 €/ton_{CO2}	−91.5%		−62.9%	
With CCS + Carbon tax 100 €/ton_{CO2} + Fuel cost + 300% ref. value	–		+237.1%	

different investigated cases (A.1, A.2 and B), the different configurations (REC, STIG and CC) and reactor arrangements (single and multireactor). $LCOE_{system}$ is obtained as the sum of $LCOE_{cycle}$ (related to thermodynamic cycle cost), $LCOE_{reactor}$ (related to reactor cost) and OPEX (both fixed and variable related to the gas cycle and fixed related to the ORC) and thus excluding the charging cost. As can be seen in Table 12 for the single reactor scheme, the lowest calculated $LCOE_{system}$ corresponds to the STIG configuration in all cases. However, the additional use of water may discourage the use of this cycle configuration, as discussed in Section 4.1. Therefore, REC configuration with a VS shaft is identified as the most promising process scheme for single reactor applications, having $LCOE_{system}$ only 2–3% higher than STIG configuration and 18% lower than CC configuration, where the higher cost associated to the ORC unit are not compensated by a sufficient increase of energy output. Case B adopting green hydrogen in charging process and Fe/Fe_2O_3 based reactor is the most economic case thanks to the higher storage energy density and the lower $LCOE_{reactor}$. Similarly for Cases A the use of iron-based oxygen carrier materials (cases A.1) results in the most affordable solution, leading to reductions in $LCOE_{system}$ larger than 4% with respect to reactors using nickel solids where the larger energy density (+80%) cannot compensate the cost increase due to material cost. The same trends are found for the investigated multireactor configuration (see Table 12), with VS shaft REC cases using iron-based materials leading to lower $LCOE_{system}$ values: final values are however higher than in the single case both because of the higher cost of the storage that is formed by smaller reactors that cannot fully exploit scale economies and the lower storage final depth of discharge due to the goal of operating the power block at stable power output.

Fig. 12 reports the final LCOE including also charging cost. Analysis is extended to larger energy storage systems (up to 500MWh) considering for the single case the adoption of different reactors deployed in series (from 1 reactor as discussed in section 4.1 to 4) while for the multireactor case a different number of reactors in parallel (from 10 as discussed in section 4.2 to 20). For Case A.1 it is possible to highlight that with biofuels and cheap natural gas it is possible to reach LCOE of around 200 €/MWh_{el} for the single reactor case, and values around 100 €/MWh for larger systems. If CCS is implemented and CT is considered for savings related to avoided CO_2 emissions, then the LCOE can be reduced in the range 60–160 €/MWh_{el}. Peak price of natural gas in 2022, also in presence of very favorable CT, leads to a strong LCOE cost increase with final values ranging between 225 and 325 €/MWh depending on storage capacity. Case A.2 implies an increase of LCOE between 10 and 30€/MWh_{el} depending on storage capacity and fuel cost confirming that the use of Ni-based oxygen carries materials is not preferable with respect to the use of Fe-based case (Case A.1). Conclusions for Case B are rather similar with the main difference that the minimum achievable LCOE, in spite of the lower $LCOE_{system}$, is very high according to the values for charging cost (above 60 €/MWh_{el} in the reference scenario). Considering cheap electricity and future PEM electrolyzer cost, the final LCOE can be reduce in the range 125–220 €/MWh_{el}. The adoption of a multireactor configuration, with the simplified management strategies proposed in this work, involves an increase of LCOE between 10 and 20€/MWh_{el} depending on the Case and the storage capacity, without penalizing excessively the economic performance of the system but unlocking the possibility to provide highly remunerated services on the balancing market. At current component costs, the proposed solution can be competitive against vanadium redox flow batteries (350–400 €/MWh_{el}), Lithium-ion batteries (300–330 €/MWh_{el}) and lead acid batteries (200 €/MWh_{el}) but without the issues related to ageing, wearing, reduced performance and limited lifetime that characterize electrochemical batteries. Moreover, the proposed technology can potentially provide an interesting alternative for long duration seasonal storage applications if the reactors could be emptied and refilled using material stored in inexpensive solid vessels at ambient temperature, whilst dramatically reducing the number of reactors. The proposed CLC concept could be also applied to decarbonization of other sectors, like naval freight transportation. In this case, reactors could be exploited in a power cycle where the turbomachinery shaft is connected (directly with a gearbox or indirectly through a generator-motor system) to the ship propeller. The use of a multireactor configuration would

Table 11
Charging cost of CASE B adopting green hydrogen.

Fuel	**Green H_2**			
Oxygen Carrier	Fe			
Δh_{ratio}	0.896			
Storage capacity, MWh_{th}	125	250	375	500
c_{ES} ref. case for 300 cycle a year (€/MWh_{th})	72.4	68.0	65.8	64.3
Relative c_{ES} variation with respect to reference case				
Cost of electricity + 50%	+26.5%	+28.2%	+29.2%	+29.8%
Cost of PEM at 2050	−26.1%	−24.2%	−23.1%	−22.4%
Modular 1 MW PEM	+36.7%	+45.5%	+50.5%	+53.9%

Table 12
$LCOE_{system}$ breakdown for seven selected CLC system configurations.

Stored energy	**125 MWh_{th}**			**250 MWh_{th}**						
Reactors operation	**Single reactor**			**2 reactors in series 125 MWh each**			**10 reactors in parallel 25 MWh each**			
Shaft	VS			VS			VS		CS	
Plant type	REC	STIG	CC	REC	STIG	CC	REC	CC	REC	CC
$LCOE_{cycle}$, €/MWh	120.5	117.9	140.7	60.2	59.0	70.3	67.8	77.5	82.8	89.9
$LCOE_{reactor}$ A.1 (Fe), €/MWh	31.9	31.1	28.8	31.9	31.1	28.8	49.6	43.8	49.5	43.5
$LCOE_{reactor}$ A.2 (Ni), €/MWh	39.8	38.9	35.9	39.8	38.9	35.9	61.8	54.6	61.7	54.2
$LCOE_{reactor}$ B (Fe), €/MWh	14.4	14.0	13.0	14.4	14.0	13.0	22.3	19.71	22.3	19.6
$LCOE_{OPEX}$, €/MWh	8.6	8.3	13.6	4.6	4.5	6.5	5.1	7.8	5.2	7.7
$LCOE_{system}$ CASE A.1 (Fe)	161	157.3	183.1	96.7	94.6	105.6	122.5	129.1	137.5	141.1
$LCOE_{system}$ CASE A.2 (Ni)	168.9	165.1	190.2	104.6	102.4	112.7	134.7	139.9	149.7	151.8
$LCOE_{system}$ CASE B (Fe)	143.5	140.2	167.3	79.2	77.5	89.8	95.2	105.0	110.3	117.2

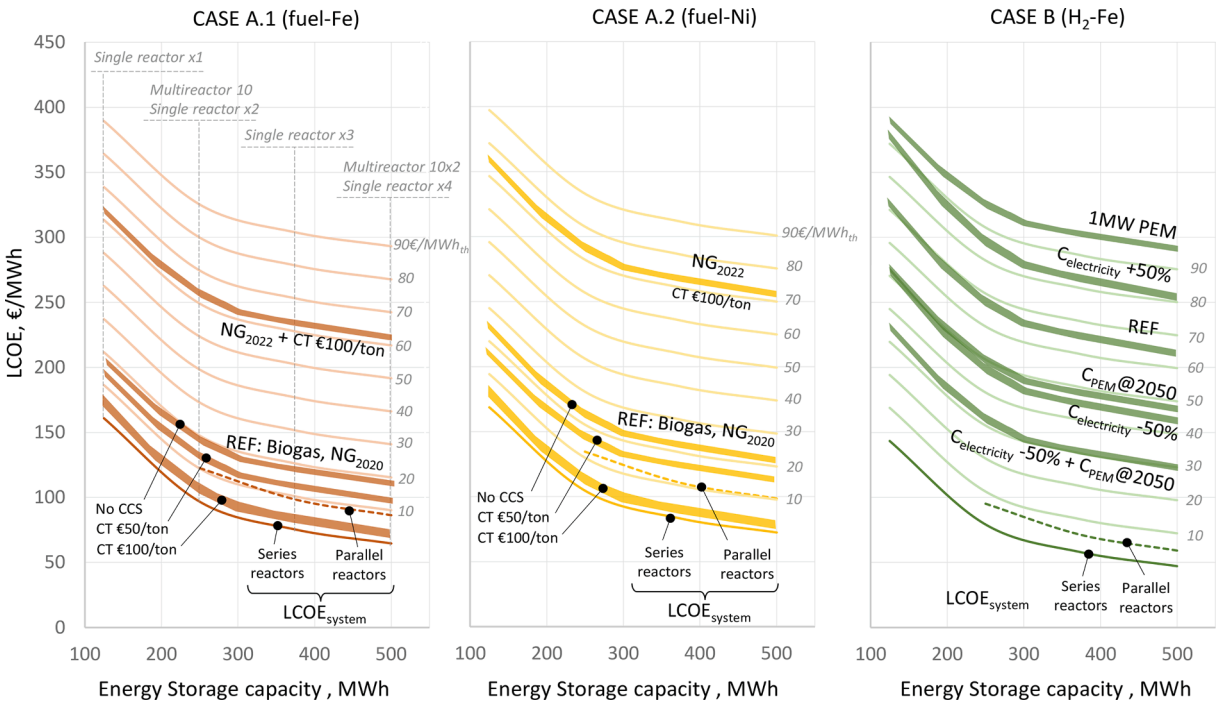

Fig. 12. Analysis of LCOE for the REC configuration with VS shaft for a) Case A.1 (Fe) b) Case A.1 (Ni) and c) Case B. In each chart the lower continuous line refers to the single reactor case $LCOE_{system}$ (and single reactors in series for larger capacity) while other continuous lines refer to the final LCOE attainable with different charging costs (c_{ES}) for the single reactor case. Colored areas highlight the final LCOE depending on the charging cost according to the sensitivity analysis proposed. Dotted line refers to the multi reactor case $LCOE_{system}$.

allow to have a flexible power system able to vary propeller speed in a relevant range but also to keep the cruise speed stable. However, a techno-economic analysis of these options if considered out of the scope of the present work.

5.4. System layout

Finally layout arrangement of the plant based on volume calculations is proposed in Fig. 13 for the multireactor case in recuperative configuration. The ten reactors are displayed in a U-tube arrangement to have the inlet and outlet manifold on the same energy storage side and reducing piping length (as well as the length occupied by the reactors). Air after intake filtering section enters the compressor and is then sent (light blue piping) to the recuperator mounted on the top of turbomachinery, as proposed by Mercury 50 assembly [76]. Heated air exiting from the recuperator flows (through the yellow piping) towards the energy storage reactor system, where it is split and fed to the active reactors by controlled valves. Air is collected at reactor exit at high temperature and sent back to the power plant (red piping), where it is expanded, cooled in the recuperator and released to the environment at the stack. Estimated land occupation is around 400 m^2. This value increases by at least a factor 2.5 in Case B to account for the electrolyzer island, which has an overall footprint of around 700 m^2 for a 30 MW system made by 5 MW PEM modules and all the required equipment [87].

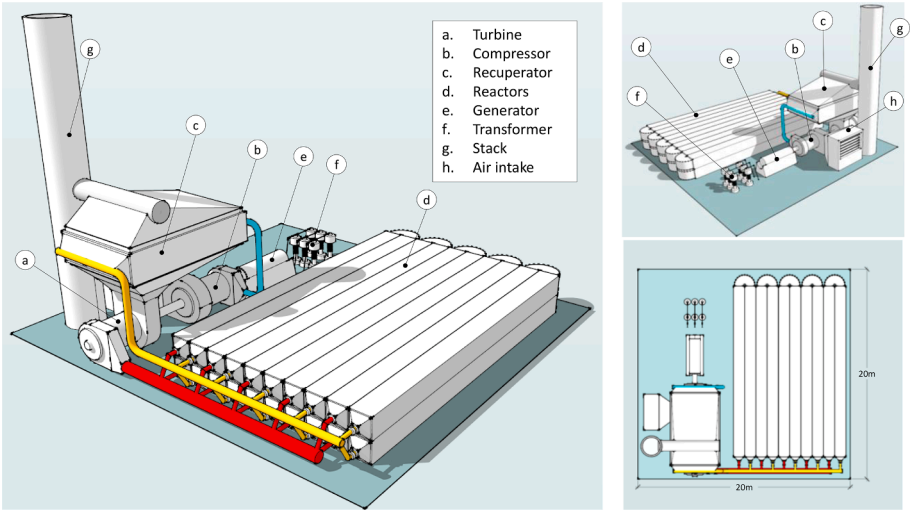

Fig. 13. Layout of a REC plant configuration in multireactor arrangement.

6. Conclusions

This paper focused on the techno-economic viability of a novel CLC reactor concept for back-up/energy storage uses integrated with a gas power cycle. The paper deals with all the relevant aspects related to the design, the performance evaluation and the economical assessment of this technology through the implementation of ad hoc models for the characterization of the reactor behavior, the power plant design optimization with integrated off design analysis, the definition of heuristic strategies for the multi reactor management and the comparison based on LCOE against other energy storage technologies. The main outcomes of this work are listed below:

- High energy densities between ~ 800 and 2200 kWh_{th}/m^3 can be attained in the reactor when using iron- or nickel-based oxygen carrier materials, providing capability for decarbonization of energy production or renewable energy storage while at the same time being able to provide a control of the air flow outlet temperature thanks to the diffusionaly based process;
- Successful integration of the reactor in recuperative, steam injected gas turbine and combined power cycles is possible in both the single and multireactor cases, achieving cycle efficiencies up to 44–49%. However, the use of STIG cycles is not recommended due to the increase in complexity and operative costs related to water consumption with respect to the recuperative system, which are not sufficiently compensated by the modest efficiency gain.
- The use of a VS shaft compressor is the preferred option in the single reactor configuration to manage the unavoidable decay in reactor power output during discharge, whilst ensuring deep reactor discharge.
- Larger flexibility can be achieved when using a multireactor configuration, allowing a nearly-constant power output to be sustained for more than 4 h under the investigated conditions. Deep reactor discharge can be attained in both the VS and CS multireactor cases, with the former providing additional flexibility during discharge.
- A preliminary economic analysis of these systems indicates that the LCOE associated to the process is largely affected by the specific cost of the fuel used during the reduction stage. The use of Iron solids as oxygen carrier material leads to more competitive values than the Nickel-based cases under the assumptions considered, with LCOE ranging between ~ 125 and 200 €/MWh_{el} when using biogas or natural gas for the charge stage, which can be even reduced down to 60€/MWh_{el} in case of high carbon tax values. If the reactor is used for renewable energy storage as an alternative to the storage of pressurized or liquefied hydrogen, LCOE increases up to ~ 215–320 €/MWh_{el} due to the large investment cost associated to the PEM electrolyzer and thus, the higher charging cost.
- The results obtained in this work show that the proposed concept for back-up power and energy storage can be competitive against electrochemical energy storage options (batteries), also providing additional lifetime advantages.

Next step of this study will focus on alternative uses for long duration energy storage adopting refillable reactors and decarbonization of the freight transport sector.

CRediT authorship contribution statement

M. Astolfi: Methodology, Software, Writing – original draft, Visualization. **M.E. Diego:** Methodology, Software, Writing – original draft. **M. Romano:** Conceptualization, Writing – review & editing, Supervision. **J.C. Abanades:** Conceptualization, Writing – review & editing, Supervision.

Declaration of Competing Interest

The authors declare the following financial interests/personal relationships which may be considered as potential competing interests: Maria Elena Diego reports financial support was provided by Spanish MICINN.

Data availability

Data will be made available on request.

Acknowledgements

The authors of this paper would like to thank Politecnico di Milano Master students (in alphabetical order) Roberto Bottino, Luca Fascia and Niccolò Guazzi who have contributed with their master thesis activities to the preliminary analysis of the system and the thermodynamic optimization of different cases. The financial support from the Spanish MICINN (PID2020-117866RJ-I00) is also gratefully acknowledged

Appendix

A.1. Table of coefficients for reactor correlations

Table A.1
Coefficients to be adopted for the calculation of $Q_{reaction}$ and Q_{gas} as function of independent parameters.

term	$Q_{reaction}$	Q_{gas}	term	$Q_{reaction}$	Q_{gas}
intercept	−21.1	−31.3	$T_{gas,in}$	$2.65{\cdot}10^{-2}$	$2.43{\cdot}10^{-2}$
$\ln(SOC)$	76.4	73.5	$\ln(SOC)\cdot(x_{O2,in})$	$-3.84{\cdot}10^{2}$	$-3.66{\cdot}10^{2}$
$(SOC)^{0.5}$	−62.7	−58.0	$(SOC)^{0.5}\cdot(x_{O2,in})$	$2.08{\cdot}10^{2}$	$1.80{\cdot}10^{2}$
SOC	3.18	2.89	$(SOC)^{0.5}\cdot(x_{O2,in})^2$	$5.11{\cdot}10^{2}$	$5.25{\cdot}10^{2}$
$(SOC)^2$	$1.77{\cdot}10^{-2}$	$1.54{\cdot}10^{-2}$	$(SOC)\cdot(x_{O2,in})$	−4.92	−3.31
$(SOC)^{2.5}$	$-3.84{\cdot}10^{-3}$	$-3.58\cdot10^{-3}$	$(SOC)\cdot(x_{O2,in})^2$	−58.7	−58.4
$(SOC)^3$	$1.97{\cdot}10^{-4}$	$1.84{\cdot}10^{-4}$	$(SOC)^2\cdot(x_{O2,in})^2$	$2.42\cdot10^{-1}$	$2.27\cdot10^{-1}$
$x_{O2,in}$	$5.35{\cdot}10^{2}$	$5.68{\cdot}10^{2}$	$\ln(SOC)\cdot\ln(m_{gas,in})$	$-2.31\cdot10^{-1}$	$-2.87\cdot10^{-1}$
$(x_{O2,in})^2$	$-1.11{\cdot}10^{3}$	$-1.16{\cdot}10^{3}$	$(SOC)^2\cdot\ln(m_{gas,in})$	$-1.03\cdot10^{-4}$	$-7.78\cdot10^{-4}$
$(m_{gas,in})^{0.5}$	−2.92	−2.31	$\ln(SOC)\cdot\ln(T_{gas,in})$	$6.71\cdot10^{-1}$	$6.16\cdot10^{-1}$
$m_{gas,in}$	$8.83{\cdot}10^{-2}$	$6.83{\cdot}10^{-2}$	$(SOC)\cdot(T_{gas,in})$	$2.85\cdot10^{-5}$	$3.48\cdot10^{-5}$
$(T_{gas,in})^{0.5}$	$3.38{\cdot}10^{-1}$	$4.23{\cdot}10^{-1}$	$(SOC)^2\cdot(T_{gas,in})^{0.5}$	$1.35\cdot10^{-4}$	$1.27\cdot10^{-4}$

A.2. Off-design resolution scheme

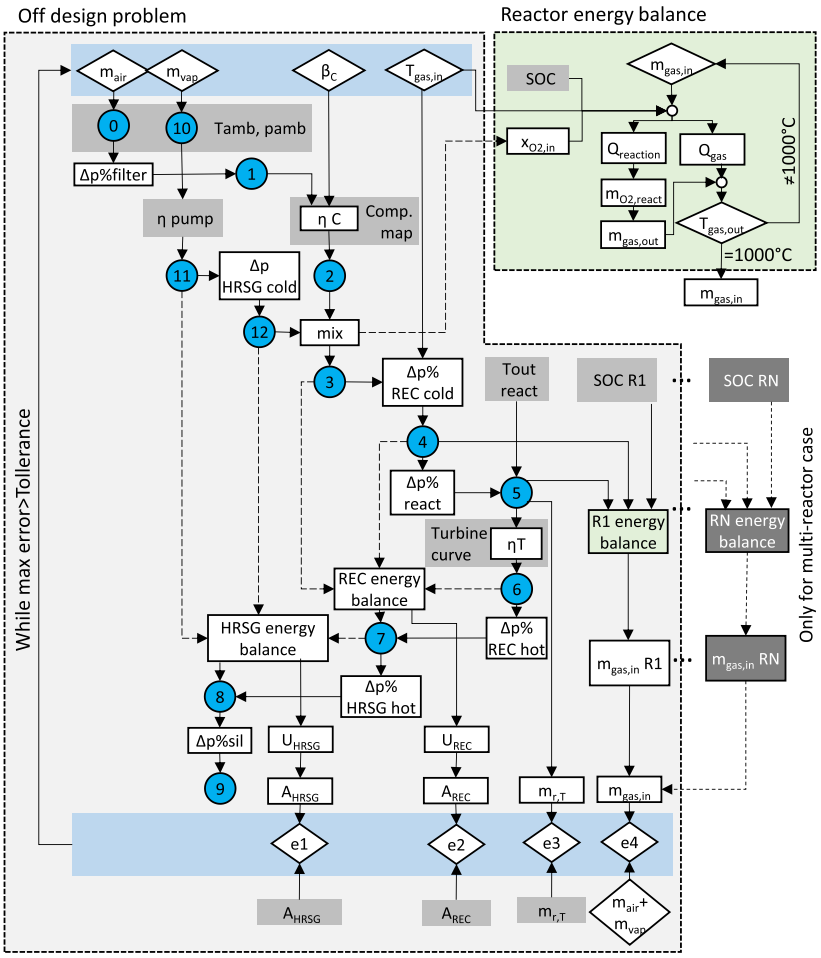

Fig. A2. Off-design numerical routine for the stig cycle showing the interdependency among the different thermodynamic points, assumptions and calculated quantities.

Thermodynamic points calculation procedure

$$T_0 = T_{amb},\ p_0 = p_{amb},\quad h_0 = h(T_0, p_0, air),\ s_0 = s(T_0, p_0, air)$$

$$T_1 = T(p_1, h_1, air),\ p_1 = p_{amb} - \Delta p_{filter},\ h_1 = h_0,\ s_1 = s(T_1, p_1, air)$$

$$T_{2is} = T(p_{2is}, s_{2is}, air),\quad p_{2,is} = p_1 \cdot \beta_C,\ h_{2,is} = h\left(p_{2,is}, s_{2,is}, air\right),\ s_{2,is} = s_1$$

$$T_2 = T(p_2, h_2, air),\quad p_2 = p_{2is},\ h_2 = h_1 + \frac{h_{2is} - h_1}{\eta_C},\quad s_2 = s(p_2, h_2, air)$$

$$T_{10} = T_{amb},\ p_{10} = p_{amb},\quad h_{10} = h(T_{10}, p_{10}, w),\ s_{10} = s(T_{10}, p_{10}, w)$$

$$T_2 = T\left(p_{12}, x_{vap} = 1, w\right),\quad p_{12} = p_2,\ h_{12} = h\left(p_{12}, x_{vap} = 1, w\right),\quad s_{12} = s(p_{12}, x_{vap} = 1, w)$$

$$T_{11is} = T(p_{11is}, s_{11is}, w),\ p_{11is} = p_{12} + \Delta p_{HRSGcold},\ h_{11is} = h(p_{11is}, s_{11is}, w),\quad s_{11is} = s_{10}$$

$$T_{11} = T(p_{11}, h_{11}, w),\quad p_{11} = p_{11is},\ h_{11} = h_{10} + \frac{h_{11is} - h_{10}}{\eta_p},\quad s_{11} = s(p_{11}, h_{11}, w)$$

$$m_{mix,in} = m_{air} + m_{vap},\ composition\,(mix_{in})$$

$$T_3 = T(p_3, h_3, mix_{in}),\ p_3 = p_2 = p_{12},\ h_3 = \frac{h_2 \cdot m_{air} + h_{12} \cdot m_{vap}}{m_{mix,in}},\quad s_3 = s(p_3, h_3, mix_{in})$$

$$T_4 = T_{gas,in},\ p_4 = p_3 - \Delta p_{RECcold},\ h_4 = h(T_4, p_4, mix_{in}),\quad s_4 = s(T_4, p_4, mix_{in})$$

$$m_{mix,out} = m_{mix,in} - m_{O2,react},\ m_{O2,react} = \sum_{i}^{n=reactors} f\left(SOC,\ T_4,\ x_{O2(mix_{in})}\right),\ composition\ (mix_{out})$$

$$T_5 = T_{out,react},\ p_5 = p_5 - \Delta p_{react},\ h_5 = h(T_5, p_5, mix_{out}),\quad s_4 = s(T_4, p_4, mix_{out})$$

$$T_{6is} = T(p_{6is}, h_{6is}, mix_{out}),\quad p_{6is} = p_0 + \Delta p_{sil} + \Delta p_{HRSGhot} + \Delta p_{REChot},\ h_{6is} = h(p_{6is}, s_{6is}, mix_{out}),\quad s_{6is} = s_5$$

$$T_6 = T(p_6, h_6, mix_{out}),\quad p_6 = p_{6is},\ h_6 = h_5 - (h_{2is} - h_1)\cdot\eta_T,\quad s_6 = s(p_6, h_6, mix_{out})$$

$$T_7 = T(p_7, h_7, mix_{out}),\quad p_7 = p_6 - \Delta p_{REChot},\ h_7 = h_6 - \frac{(h_4 - h_3)\cdot m_{mix,in}}{m_{mix,out}},\quad s_7 = s(p_7, h_7, mix_{out})$$

$$T_8 = T(p_8, h_8, mix_{out}),\quad p_8 = p_7 - \Delta p_{HRSGhot},\ h_8 = h_7 - \frac{(h_{12} - h_{11})\cdot m_{vap}}{m_{mix,out}},\quad s_8 = s(p_8, h_8, mix_{out})$$

$$T_9 = T(p_9, h_9, mix_{out}),\ p_9 = p_8 - \Delta p_{sil} = p_0,\ h_9 = h_8,\ s_9 = s(p_9, h_9, mix_{out})$$

$$A = \frac{1}{U}\sum_{i=1}^{n}\frac{\Delta Q_i}{\Delta T_{mln,i}},\ \Delta T_{mln,i} = \frac{\Delta T_{hotend,i} - \Delta T_{coldend,i}}{ln\frac{\Delta T_{hotend,i}}{\Delta T_{coldend,i}}},\ for\ HRS\ and\ REC,\ n\ number\ of\ nodes$$

Notes:

- relative pressure drops are reported in equations as absolute values for clarity and are calculated with reference to the inlet pressure as $\Delta p = p_{in}\cdot\Delta p_{\%}$
- mix_{in}: composition of the stream resulting from mixing of m_{air} and m_{vap} at reactor inlet
- mix_{out}: composition of the stream released from the reactor and determined by reacted m_{O2}

A.3. cost correlations for power plant components

Cost correlations are reported in Table A.2 with the estimated equipment cost for the recuperative cycle with variable speed compressor equipment. It is possible to note that the available correlations [62–64] result in turbine and compressor costs in a wide range equal to 9–20 M€$_{2020}$ and 1.2–26 M€$_{2020}$ respectively leading to a high uncertainty on the final system cost evaluation. The recuperator is another component with a high cost uncertainty related to the high variability of the global heat transfer coefficient and the different specific cost of different type of heat exchangers (S&T, plate& fin, finned tube battery, etc). Cost correlations are available from different references focused on gas cycles [62,64] and on general process heat exchangers [65,71]. A relatively good agreement is obtained by Arsalis (2005) [64] and ESDU report [65] (adopting plate and fin heat exchanger with$U$ = 100 W/Km^2) leading to recuperator cost respectively equal to 2.4 M€2020 and 1.7 M€$_{2020}$ while Loh (2002) [71] correlation results in a higher cost (6.8 M€$_{2020}$) but considering S&T heat exchanger with no scale economy due to system modularity above 6500 m^2, finally Valero correlation confirms to be the most conservative one (14.6 M€$_{2020}$).

Table A.2
Cost correlations from literature for main power cycle equipment and cost evaluation for the recuperative cycle with variable speed compressor.

reference	Original cost correlation	unit	Inflation factor	cost M€2020
Turbine				
Valero [62]	$\frac{266.3 m_{in}}{0.92-\eta}\ln(\beta)\left(1+e^{(0.0036T_{in}-54.4)}\right)$	$	1.79	19
El-Sayed [63]	$7263 m_{in}\beta^{0.5}\left(\frac{\eta}{1-\eta}\right)^{0.85}$	$	1.44	8.7
Arsalis [64]	$(-98.328\ln(W_{el})+1318.5)W_{el}$	$	1.37	10
Compressor				
Valero [62]	$\frac{39.5 m_{in}}{0.90-\eta}\ln(\beta)$	$	1.79	25.77
El-Sayed [63]	$3389.4 m_{in}\beta^{0.45}\left(\frac{\eta}{1-\eta}\right)^{0.45}$	$	1.44	2.57
Arsalis [64]	$91562\left(\frac{W_{el}}{445}\right)^{0.67}$	$	1.37	1.26
Recuperator				
Valero [62]	$2290A^{0.6}$	$	1.79	14.57
Arsalis [64]	$130\left(\frac{A}{0.093}\right)^{0.78}$	$	1.37	2.45
ESDU [65]	$0.327UA$	£	2	1.70
Loh [71]	$1450\left(\frac{A}{6.50}\right)$	$	1.59	6.81

Excluding the correlation set from Valero (1994) [62] (then also used by Bejan (1996) [66] and Siahaya (2009) [67]) which results in a large overestimation of system cost the other proposed correlations from literature are relatively in good agreement considering that any cost estimation has an uncertainty as large as ± 20–30% and that the reliability of cost correlations reduces over time. For equipment cost estimation the correlations from Y. M. El-Sayed (2003) [63] have been preferred to Arsalis (2005) [64] for expander and compressor since they includes the effect of mass flow rate, pressure ratio and efficiency while the cost correlation from Arsalis (2005) [64] has been adopted for the recuperator because it is the most recent one.

References

[1] Davis SJ, et al. Net-zero emissions energy systems. Science (1979) 2018;360(6396). 10.1126/SCIENCE.AAS9793/SUPPL_FILE/AAS9793-DAVIS-SM.PDF.

[2] I. Renewable Energy Agency. Innovation landscape for a renewable-powered future: solutions to integrate variable renewables; 2019, Accessed: Feb. 06, 2023. [Online]. Available: www.irena.org/publications.

[3] World Energy Outlook 2022 – Analysis - IEA. Accessed: Feb. 06, 2023. [Online]. Available: https://www.iea.org/reports/world-energy-outlook-2022.

[4] Lund H, Salgi G. The role of compressed air energy storage (CAES) in future sustainable energy systems. Energy Convers Manag May 2009;50(5):1172–9. https://doi.org/10.1016/J.ENCONMAN.2009.01.032.

[5] Astolfi M, Guandalini G, Belloli M, Hirn A, Silva P, Campanari S. Preliminary design and performance assessment of an underwater compressed air energy storage system for wind power balancing. J Eng Gas Turbine Power Sep. 2020;142 (9). https://doi.org/10.1115/1.4047375/1084126.

[6] Guizzi GL, Manno M, Tolomei LM, Vitali RM. Thermodynamic analysis of a liquid air energy storage system. Energy 2015;93:1639–47. https://doi.org/10.1016/j.energy.2015.10.030.

[7] Astolfi M, Rizzi D, Macchi E, Spadacini C. A Novel Energy Storage System Based on Carbon Dioxide Unique Thermodynamic Properties. J Eng Gas Turbine Power Aug. 2022;144(8). https://doi.org/10.1115/1.4054750/1141484.

[8] "Home | Malta." https://www.maltainc.com/ [accessed Feb. 06, 2023].

[9] Mercangöz M, Hemrle J, Kaufmann L, Z'Graggen A, Ohler C. Electrothermal energy storage with transcritical CO2 cycles. Energy Sep. 2012;45(1):407–15. https://doi.org/10.1016/J.ENERGY.2012.03.013.

[10] Alfani D, Giostri A, Astolfi M. Working fluid selection and thermodynamic optimization of the novel renewable-energy based restore seasonal storage technology. *Proceedings of ASME Turbo Expo 2023: Turbine Technical Conference and Exposition - paper under review*; 2023. p. 1–12.

[11] Gallo AB, Simões-Moreira JR, Costa HKM, Santos MM, Moutinho dos Santos E. Energy storage in the energy transition context: A technology review. Renew Sustain Energy Rev Nov. 2016;65:800–22. https://doi.org/10.1016/J.RSER.2016.07.028.

[12] Koohi-Fayegh S, Rosen MA. A review of energy storage types, applications and recent developments. J Energy Storage Feb. 2020;27:101047. https://doi.org/10.1016/J.EST.2019.101047.

[13] Yang Z, et al. Electrochemical energy storage for green grid. Chem Rev May 2011; 111(5):3577–613. https://doi.org/10.1021/CR100290V/ASSET/IMAGES/CR-2010-00290V_M026.GIF.

[14] Siemens. Power-to-X: The crucial business on the way to a carbon-free world. *Technial Paper Siemens AG*; 2019. p. 1–26.

[15] SAPEA. Science Advice for Policy by European Academies Novel carbon capture and utilisation technologies Research and climate aspects. doi: 10.26356/CARBONCAPTURE.

[16] Abanades JC, Rubin ES, Mazzotti M, Herzog HJ. On the climate change mitigation potential of CO2 conversion to fuels. Energy Environ Sci Dec. 2017;10(12):2491–9. https://doi.org/10.1039/C7EE02819A.

[17] Lyngfelt A. Chemical looping combustion (CLC). Fluidized Bed Technologies for Near-Zero Emission Combustion and Gasification 2013:895–930. https://doi.org/10.1533/9780857098801.4.895.

[18] Adanez J, Abad A, Garcia-Labiano F, Gayan P, de Diego LF. Progress in chemical-looping combustion and reforming technologies. Prog Energy Combust Sci Apr. 2012;38(2):215–82. https://doi.org/10.1016/J.PECS.2011.09.001.

[19] Aghaie M, Mehrpooya M, Pourfayaz F. Introducing an integrated chemical looping hydrogen production, inherent carbon capture and solid oxide fuel cell biomass fueled power plant process configuration. Energy Convers Manag Sep. 2016;124: 141–54. https://doi.org/10.1016/J.ENCONMAN.2016.07.001.

[20] Rajabi M, Mehrpooya M, Haibo Z, Huang Z. Chemical looping technology in CHP (combined heat and power) and CCHP (combined cooling heating and power) systems: A critical review. Appl Energy Nov. 2019;253:113544. https://doi.org/10.1016/J.APENERGY.2019.113544.

[21] Wu S, Zhou C, Doroodchi E, Nellore R, Moghtaderi B. A review on high-temperature thermochemical energy storage based on metal oxides redox cycle. Energy Convers Manag Jul. 2018;168:421–53. https://doi.org/10.1016/J.ENCONMAN.2018.05.017.

[22] Bergthorson JM, et al. Direct combustion of recyclable metal fuels for zero-carbon heat and power. Appl Energy Dec. 2015;160:368–82. https://doi.org/10.1016/J.APENERGY.2015.09.037.

[23] Bergthorson JM. Recyclable metal fuels for clean and compact zero-carbon power. Prog Energy Combust Sci Sep. 2018;68:169–96. https://doi.org/10.1016/J.PECS.2018.05.001.

[24] Abad A, et al. Evaluation of the redox capability of manganese–titanium mixed oxides for thermochemical energy storage and chemical looping processes. Fuel Process Technol Jan. 2021;211:106579. https://doi.org/10.1016/J.FUPROC.2020.106579.

[25] Yilmaz D, Darwish E, Leion H. Investigation of the combined Mn-Si oxide system for thermochemical energy storage applications. J Energy Storage Apr. 2020;28: 101180. https://doi.org/10.1016/J.EST.2019.101180.

[26] Wu S, Zhou C, Doroodchi E, Moghtaderi B. A unique phase change redox cycle using CuO/Cu2O for utility-scale energy storage. Energy Convers Manag May 2019;188:366–80. https://doi.org/10.1016/J.ENCONMAN.2019.03.055.

[27] Galvita VV, Poelman H, Marin GB. Combined chemical looping for energy storage and conversion. J Power Sources Jul. 2015;286:362–70. https://doi.org/10.1016/J.JPOWSOUR.2015.03.183.

[28] Cormos CC, Dragan S, Cormos AM, Petrescu L. Assessment of Flexible Thermochemical Energy Conversion and Storage System based on Chemical Looping Combustion. Chem Eng Trans Sep. 2022;94:25–30. https://doi.org/10.3303/CET2294004.

[29] Bock S, Pauritsch M, Lux S, Hacker V. Natural iron ores for large-scale thermochemical hydrogen and energy storage. Energy Convers Manag Sep. 2022; 267:115834. https://doi.org/10.1016/J.ENCONMAN.2022.115834.

[30] Yan Y, Wang K, Clough PT, Anthony EJ. Developments in calcium/chemical looping and metal oxide redox cycles for high-temperature thermochemical energy storage: A review. Fuel Process Technol Mar. 2020;199:106280. https://doi.org/10.1016/J.FUPROC.2019.106280.

[31] Baumann M, Barelli L, Passerini S, Baumann M, Passerini S, Barelli L. The Potential Role of Reactive Metals for a Clean Energy Transition. Adv Energy Mater Jul. 2020; 10(27):2001002. https://doi.org/10.1002/AENM.202001002.

[32] Ebadi M, Mehrpooya M, Kani AH. Sensitivity analysis and optimization of geometric and operational parameters in a thermochemical heat storage redox reactor used for concentrated solar power plants. J Therm Anal Calorim Jun. 2022; 147(11):6415–35. https://doi.org/10.1007/S10973-021-10980-3/FIGURES/17.

[33] Wentworth WE, Chen E. Simple thermal decomposition reactions for storage of solar thermal energy. Sol Energy Jan. 1976;18(3):205–14. https://doi.org/10.1016/0038-092X(76)90019-0.

[34] Bahzad H, Fennell P, Shah N, Hallett J, Ali N. Techno-economic assessment for a pumped thermal energy storage integrated with open cycle gas turbine and chemical looping technology. Energy Convers Manag Mar. 2022;255:115332. https://doi.org/10.1016/J.ENCONMAN.2022.115332.

[35] Diego ME, Abanades JC. Techno-economic analysis of a low carbon back-up power system using chemical looping. Renew Sustain Energy Rev Oct. 2020;132:110099. https://doi.org/10.1016/J.RSER.2020.110099.

[36] Abanades JC, Diego ME, Fernández JR. A novel air reactor concept for chemical looping combustion systems operated at high pressure. Chem Eng J Jun. 2020;390: 124507. https://doi.org/10.1016/J.CEJ.2020.124507.

[37] Saghafifar M, Scott SA. The use of high decomposition temperature materials for chemical looping electricity storage. Chem Eng J Nov. 2021;423. https://doi.org/10.1016/J.CEJ.2021.128789.

[38] Noorman S, van Sint Annaland M, Kuipers H. Packed bed reactor technology for chemical-looping combustion. Ind Eng Chem Res Jun. 2007;46(12):4212–20. https://doi.org/10.1021/IE061178I/ASSET/IMAGES/LARGE/IE061178IF00016.JPEG.

[39] Diego ME, Abanades JC. Experimental investigation of a diffusion-controlled chemical looping air reactor for energy storage applications. Chem Eng J Jan. 2022;428:132083. https://doi.org/10.1016/J.CEJ.2021.132083.

[40] Spallina V, Gallucci F, Romano MC, Chiesa P, Lozza G, van Sint Annaland M. Investigation of heat management for CLC of syngas in packed bed reactors. Chem Eng J Jun. 2013;225:174–91. https://doi.org/10.1016/J.CEJ.2013.03.054.

[41] Fernández JR, Alarcón JM. Chemical looping combustion process in fixed-bed reactors using ilmenite as oxygen carrier: Conceptual design and operation strategy. Chem Eng J Mar. 2015;264:797–806. https://doi.org/10.1016/J.CEJ.2014.12.022.

[42] Jerndal E, Mattisson T, Lyngfelt A. Thermal Analysis of Chemical-Looping Combustion. Chem Eng Res Des Sep. 2006;84(9):795–806. https://doi.org/10.1205/CHERD05020.

[43] Baiocchi G, Distaso W. GRETL: Econometric software for the GNU generation. J Appl Economet Jan. 2003;18(1):105–10. https://doi.org/10.1002/JAE.704.

[44] "MATLAB R2022a, The MathWorks, Inc., Natick, Massachusetts, United States.".

[45] Singh K. Advanced Materials for Land Based Gas Turbines. Trans Indian Inst Met Oct. 2014;67(5):601–15. https://doi.org/10.1007/S12666-014-0398-3/FIGURES/16.

[46] Gómez-Aláez SL, Brizzi V, Alfani D, Silva P, Giostri A, Astolfi M. Off-design study of a waste heat recovery ORC module in gas pipelines recompression station. Energy Procedia 2017;129:567–74. https://doi.org/10.1016/J.EGYPRO.2017.09.205.

[47] Lemmon EW, Bell IH, Huber ML, McLinden MO. NIST Standard Reference Database 23: Reference Fluid Thermodynamic and Transport Properties-REFPROP, Version 10.0, National Institute of Standards and Technology, Standard Reference Data Program. Gaithersburg; 2018.

[48] Tomita JT, Barbosa JR. A model for numerical simulation of variable stator axial flow compressors; 2003.

[49] Johnson IA, Bullock RO. Aerodynamic Design of Axial-Flow Compressors; 1965.

[50] Converse GL, Giffin RG. Extended parametric representation of compressor fans and turbines. Volume 1: CMGEN user's manual; 1984.

[51] Liu Z, Karimi IA. Simulation and optimization of a combined cycle gas turbine power plant for part-load operation. Chem Eng Res Des Mar. 2018;131:29–40. https://doi.org/10.1016/J.CHERD.2017.12.009.

[52] Theodore DPD, Bergman L, Lavine Adrienne S, Incropera Frank P. Fundamentals of Heat and Mass Transfer, 8th Edition; 2018. p. 992, Accessed: Feb. 06, 2023. [Online]. Available: https://www.wiley.com/en-us/Fundamentals+of+Heat+and+Mass+Transfer%2C+8th+Edition-p-9781119353881.

[53] Turboden. Turboden Solutions For Industrial Processes. [Online]. Available: https://www.turboden.com/download_file_cta.php?id_ref=3008&lang=ITA.

[54] Audet C, Dennis JE. Analysis of Generalized Pattern Searches. 2006;13(3): 889–903. doi: 10.1137/S1052623400378742.

[55] Kallrath J. Combined strategic and operational planning - An MILP success story in chemical industry. OR Spectr 2002;24(3):315–41. https://doi.org/10.1007/S00291-002-0102-6/METRICS.

[56] Macchi E, Astolfi M. Organic Rankine Cycle (ORC) Power Systems. *Organic Rankine Cycle (ORC)* Power Syst 2017. https://doi.org/10.1016/C2014-0-04239-6.

[57] Zakeri B, Syri S. Electrical energy storage systems: A comparative life cycle cost analysis. Renew Sustain Energy Rev Feb. 2015;42:569–96. https://doi.org/10.1016/J.RSER.2014.10.011.
[58] Schmidt O, Melchior S, Hawkes A, Staffell I. Projecting the Future Levelized Cost of Electricity Storage Technologies. Joule Jan. 2019;3(1):81–100. https://doi.org/10.1016/J.JOULE.2018.12.008.
[59] Jülch V. Comparison of electricity storage options using levelized cost of storage (LCOS) method. Appl Energy Dec. 2016;183:1594–606. https://doi.org/10.1016/J.APENERGY.2016.08.165.
[60] Riva L, Martínez I, Martini M, Gallucci F, van Sint Annaland M, Romano MC. Techno-economic analysis of the Ca-Cu process integrated in hydrogen plants with CO2 capture. Int J Hydrogen Energy Aug. 2018;43(33):15720–38. https://doi.org/10.1016/J.IJHYDENE.2018.07.002.
[61] Mancuso L, Cloete S, Chiesa P, Amini S. Economic assessment of packed bed chemical looping combustion and suitable benchmarks. Int J Greenhouse Gas Control Sep. 2017;64:223–33. https://doi.org/10.1016/J.IJGGC.2017.07.015.
[62] Valero A, et al. CGAM problem: Definition and conventional solution. Energy Mar. 1994;19(3):279–86. https://doi.org/10.1016/0360-5442(94)90112-0.
[63] El-Sayed YM. The Thermoeconomics of Energy Conversions. Thermoecon Energy Convers 2003:1–264.
[64] Arsalis A. Thermoeconomic modeling and parametric study of hybrid SOFC–gas turbine–steam turbine power plants ranging from 1.5 to 10 MWe. J Power Sources Jul. 2008;181(2):313–26. https://doi.org/10.1016/J.JPOWSOUR.2007.11.104.
[65] ESDU 92013. Selection and costing of heat exchangers. Accessed: Feb. 07, 2023. [Online]. Available: https://www.esdu.com/cgi-bin/ps.pl?sess=unlicensed_1230207085239fhm&t=doc&p=esdu_92013b.
[66] Bejan A, Tsatsaronis G, Moran M. Thermal Design & Optimization. p. 542, 1996, Accessed: Feb. 07, 2023. [Online]. Available: https://www.wiley.com/en-us/Thermal+Design+and+Optimization-p-9780471584674.
[67] Siahaya Y. Thermoeconomic analysis and optimization of gas turbine power plant. In: *Proceedings of the International Conference on Fluid and Thermal Energy Conversion*, 2009. Accessed: Feb. 07, 2023. [Online]. Available: https://www.researchgate.net/publication/267780800_Thermoeconomic_analysis_and_optimization_of_gas_turbine_power_plant.
[68] Quoilin S, van den Broek M, Declaye S, Dewallef P, Lemort V. Techno-economic survey of Organic Rankine Cycle (ORC) systems. Renew Sustain Energy Rev Jun. 2013;22:168–86. https://doi.org/10.1016/J.RSER.2013.01.028.
[69] U. Environmental Protection Agency, C. Heat, and P. Partnership, "Catalog of CHP Technologies, Section 3. Technology Characterization – Combustion Turbines,"; 2015.
[70] Pauschert D. Energy Sector Management Assistance Program Study of Equipment Prices in the Power Sector; 2009.
[71] Loh HP, Lyons J, White CW. Process Equipment Cost Estimation, Final Report; Jan. 2002, doi: 10.2172/797810.
[72] Green DW, Perry RH. *Perry's Chemical Engineers' Handbook, Eighth Edition*. McGraw-Hill Education; 2008. Accessed: Feb. 06, 2023. [Online]. Available: https://www.accessengineeringlibrary.com/content/book/9780071422949.
[73] Weiland NT, Lance BW, Pidaparti SR. sCO2 Power Cycle Component Cost Correlations from DOE Data Spanning Multiple Scales and Applications. Proceedings of the ASME Turbo Expo 2019;9:Feb. https://doi.org/10.1115/GT2019-90493.
[74] Xiao G, et al. Recuperators for micro gas turbines: A review. Appl Energy Jul. 2017;197:83–99. https://doi.org/10.1016/J.APENERGY.2017.03.095.
[75] Ansaldo Energia, "AE-T100." https://www.ansaldoenergia.com/offering/equipment/turbomachinery/microturbines/ae-t-100 (accessed Feb. 06, 2023).
[76] Solar Turbines, "Mercury 50." https://www.solarturbines.com/en_US/products/power-generation-packages/mercury-50.html (accessed Feb. 06, 2023).
[77] "2022 GTW Handbook, Volume 37 - Gas Turbine World." https://gasturbineworld.com/shop/annual-handbook/2022-gtw-handbook-volume-37/ (accessed Feb. 06, 2023).
[78] I. Renewable Energy Agency, "Biogas for Road Vehicles: Technology brief," 2018.
[79] "EU: industrial natural gas prices 2020 | Statista." https://www.statista.com/statistics/1047070/natural-gas-price-european-union/ (accessed Feb. 06, 2023).
[80] "TTF gas price 2023 | Statista." https://www.statista.com/statistics/1267202/weekly-dutch-ttf-gas-futures/ (accessed Feb. 06, 2023).
[81] A. Zauner, H. Böhm, D. C. Rosenfeld, and R. Tichler, "Innovative large-scale energy storage technologies and Power-to-Gas concepts after optimization Analysis on future technology options and on techno-economic optimization," 2019.
[82] "Efficiency-Electrolysis White paper siemens-energy.com/electrolyzer," 2021.
[83] M. Hamdan, "PEM Electrolyzer Incorporating an Advanced Low-Cost Membrane," Aug. 2013, doi: 10.2172/1091385.
[84] Mayyas A, Ruth M, Pivovar B, Bender G, Wipke K. Manufacturing Cost Analysis for Proton Exchange Membrane Water Electrolyzers [Online]. Available: Accessed: Feb 2019;07:2023. https://www.nrel.gov/docs/fy10osti/72740.pdf.
[85] "The hydrogen trajectory - KPMG Belgium," Nov. 2022, Accessed: Feb. 07, 2023. [Online]. Available: https://kpmg.com/be/en/home/insights/2021/03/eng-the-hydrogen-trajectory.html.
[86] Thomas DH. Cost reduction potential for electrolyser technology. In: *Proceedings of European PowerToGas Platform*, 2017. Accessed: Feb. 07, 2023. [Online]. Available: https://youtu.be/UJXhX4dLMtA.
[87] Thomas D. Large scale PEM electrolysis: technology status and upscaling strategies; 2019. Accessed: Feb. 06, 2023. [Online]. Available: https://www.electrive.com/2019/07/01/cummins-takes-over-fuel-cell-maker-hydrogenics/.